Reactor modeling for two-step solar thermochemical fuel production: a concise review

frontiers | Frontiers in Energy Research

TYPE Review
PUBLISHED 09 February 2026
DOI 10.3389/fenrg.2025.1671615



OPEN ACCESS

EDITED BY
Michael Folsom Toney,
University of Colorado Boulder, United States

REVIEWED BY
Yihang Li,
Xidian University, China
Brendan Bulfin,
University College Cork, Ireland

*CORRESPONDENCE
Francesco Orsini,
francesco.orsini@polito.it

RECEIVED 23 July 2025
REVISED 22 September 2025
ACCEPTED 30 October 2025
PUBLISHED 09 February 2026

CITATION
Riberi M, Orsini F, Ferrero D and Santarelli M (2026) Reactor modeling for two-step solar thermochemical fuel production: a concise review.
*Front. Energy Res.* 13:1671615.
doi: 10.3389/fenrg.2025.1671615



# Reactor modeling for two-step solar thermochemical fuel production: a concise review

Matteo Riberi, Francesco Orsini*, Domenico Ferrero and Massimo Santarelli

Energy Department (DENERG), Politecnico di Torino, Corso Duca degli Abruzzi, Torino, Italy

Solar thermochemical fuel production based on the use of non-volatile, non-stoichiometric redox materials to drive water and carbon dioxide splitting in two-step redox cycles represents a promising approach for efficient solar energy conversion and storage. High theoretical solar-to-fuel efficiencies can be achieved, as reduction and oxidation of redox materials are separated, unlocking the possibility to optimize the thermodynamic conditions of each half-reaction. However, the scale-up of the technology is still hindered by low efficiencies reached by reactor prototypes. In this context, the multiphysics modeling of reactor concepts represents a key tool in the engineering process to find optimal designs and suitable operating conditions. This work presents a comprehensive literature review on reactor modeling, by identifying and discussing the most diffused modeling techniques. Our review unveiled that, in terms of heat and mass transfer modeling, most of the studies are aligned in considering laminar flow conditions and local thermal non-equilibrium between the solid and fluid phases in the reactive porous medium. On the other hand, diverse approaches were proposed to include the chemical reaction and radiative heat transfer in the reactor model. Specifically, the redox reaction is modelled either by assuming thermodynamic equilibrium or by including kinetics, with several expressions proposed up to date. The main literature gap identified in the present study is represented by the limited number of multiphysics models that integrate redox materials other than state-of-the-art ceria, as well as innovative reactor designs aiming at overcoming the main limitations of state-of-the-art systems.

KEYWORDS

**review, reactor modeling, two-step thermochemical cycles, solar fuel production, multiphysics coupling**

## 1 Introduction

During the last decades, climate change and growing greenhouse gas emissions have become pressing topics at a global scale. According to Paris Agreement and the following legislations, limiting the impact of climate change requires to reduce global greenhouse gas emissions of 45% by 2030 and reach climate neutrality by 2050 to limit the average temperature increase below 1.5 °C (United Nations, 2025). Limiting greenhouse gas emissions implies several challenges to be faced, especially in the energy sector. As stated in the World Energy Outlook presented by the International Energy Agency (IEA) in 2024, 80% of the primary energy produced nowadays comes from fossil fuels. The need for sustainable and renewable energy sources is critical, nonetheless, the

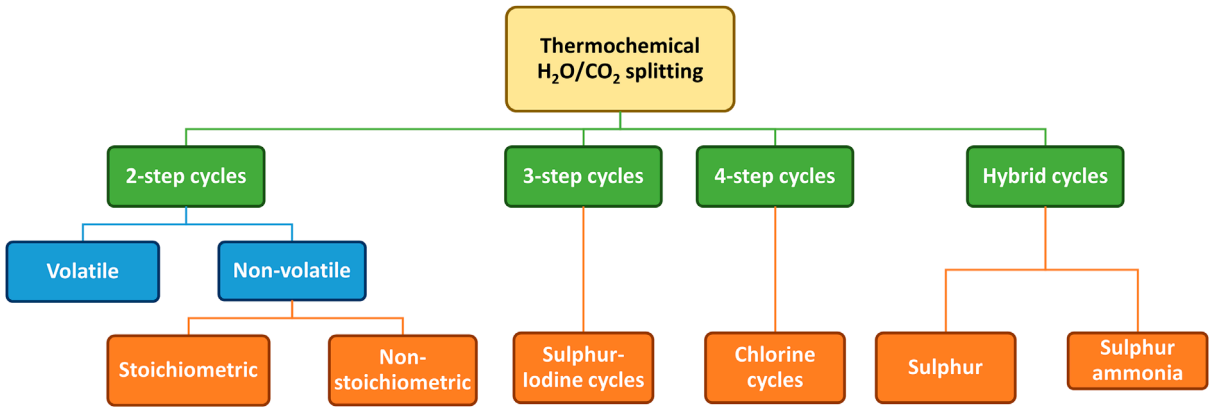


FIGURE 1
General classification of solar thermochemical cycles.

most promising sources such as solar and wind still face issues related to intermittency and storage (World Energy Outlook, 2024).

In this context, thermochemical cycles for solar fuel production represent a promising pathway for solar energy conversion and storage. By transforming solar radiation into chemical energy stored in high-energy molecules (*e.g.*, hydrogen, syngas, or other downstream synthetic fuels), they offer stable energy carriers that remain compatible with today's infrastructure, which is still largely tailored to fossil-based fuels (Guo et al., 2024). Currently, however, thermochemical $H_2O$ and $CO_2$ splitting cycles face significant performance limitations: the best demonstrations have achieved solar-to-fuel efficiencies of only 4%–6%, excluding solar collection and spillage (Zoller et al., 2022; Marxer et al., 2017; Tran et al., 2024; Wei et al., 2023). For comparison, mature photovoltaic-electrolysis systems have recently reached solar-to-hydrogen efficiencies of around 30% (Jia et al., 2016), while photo (electro) catalytic approaches have reported values above 10% (Verlage et al., 2015). Despite these drawbacks, thermochemical cycles retain unique advantages. They can, in principle, achieve higher efficiencies because high-temperature heat is directly stored in the chemical bonds of the fuel molecules, thereby avoiding intermediate energy conversion steps (Wei et al., 2023). Furthermore, by exploiting the full solar spectrum, these cycles pave the way to high conversion efficiencies, with theoretical limits estimated between 20% and 35% (Moretti et al., 2023; Lin and Haussener, 2015; Li et al., 2018).

Several chemical looping cycles for thermochemical water and carbon dioxide splitting have been proposed in the literature, with the most relevant approaches schematized in Figure 1. The general concept is based on breaking the overall $H_2O/CO_2$ splitting reaction into intermediate steps to lower the reaction temperature through the integration of suitable redox materials that enhance the reaction thermodynamics. Solutions with a larger number of intermediate steps guarantee a lower reaction temperature, but in contrast are associated with more complex systems. For a more detailed description of each option, the reader is redirected to other reviews focusing on this topic (Safari and Dincer, 2020).

Among the different solutions proposed, often addressing the water splitting as the target reaction, two-step cycles were reported to be the only option adopted so far to perform also carbon dioxide splitting (Lu et al., 2019).

In two-step thermochemical cycles, which is the focus of this review, the redox material is cycled between an endothermic reduction step, where it is reduced by abstracting oxygen from the lattice, and an exothermic oxidation step, in which it is re-oxidized by splitting the $H_2O/CO_2$ molecules and replenishing the oxygen into the lattice. According to the reduction mechanism, two-step cycles can be classified into three main categories: volatile, non-volatile stoichiometric, and non-volatile non-stoichiometric cycles (Wei et al., 2023). In the first two cases the material is completely reduced, up to undergoing a phase change (that can be solid-gas for volatile cycles, solid-liquid or solid-solid for non-volatile stoichiometric cycles) (Bulfin et al., 2017). On the other hand, in the non-stoichiometric case, only a portion of cations participate to the reaction, while the others remain in the same oxidation state. Equations 1, 2 show the reduction and oxidation reactions, respectively. This mechanism is described by the parameter $\delta$, referred to as the nonstoichiometry, quantifying the reduction extent reached at the end of the reduction step and corresponding to the moles of monoatomic oxygen vacancies generated per mole of reactive material. During this process, oxygen ions move across the lattice through the formation of oxygen vacancies, and this does not cause a phase transformation. The fact that the material remains in the same solid phase during the entire cycle ensures enhanced structural stability, making non-stoichiometric materials such as ferrites, ceria, and perovskites the most studied solution throughout the literature currently (Lu et al., 2019).

$$MO_x \rightarrow MO_{x-\delta} + \frac{\delta}{2} O_2 \tag{1}$$

$$MO_{x-\delta} + \delta H_2O\,(\delta CO_2) \rightarrow MO_x + \delta H_2\,(\delta CO) \tag{2}$$

A wide range of studies focusing on two-step thermochemical cycles for solar fuel production has been published in recent years, spanning from materials' investigation, up to reactor-level or system-level modeling. One of the most successfully demonstrated state-of-the-art reactor designs is represented by directly irradiated reactors of the cavity type, consisting of a

hollow-shaped redox material enclosed by a window transparent to concentrated radiation. The incoming radiation penetrates in the reaction chamber and directly heats the redox material positioned inside the cavity. The reactive element can be manufactured with different morphologies and materials. The most common option is the realization of reticulated porous structures, that maximize the exposed reactive surface and the radiative heat transport through the bulk. Regarding the redox material, ceria ($CeO_2$) is by far the most adopted option up to date, mainly for its good thermal stability and fast reaction kinetics (Haeussler et al., 2020a). In contrast to these benefits, efficiencies of state-of-the-art reactors are still limited–among others, due to the relatively limited reduction extent of the redox material considered. The highest solar-to-fuel efficiency reported in the literature was obtained in a directly irradiated cavity-type reactor with dual-scale porosity ceria as the redox material, for thermochemical splitting of carbon dioxide. The mentioned reactor has been experimentally demonstrated at the 4-kW and 50-kW scales, achieving solar-to-fuel efficiencies of 5.25% and 5.6%, respectively (Zoller et al., 2022; Marxer et al., 2017). Currently, the main alternative to ceria is represented by perovskites, that although providing a larger reduction extent upon reduction at more moderate temperatures thanks to a typically lower oxygen vacancy formation enthalpy, on the other hand demonstrate a poorer oxidation performance leading to higher $H_2O/CO_2$ demand and associated energy penalties (Haeussler et al., 2018). Despite the potentially promising results, comprehensive studies regarding their thermodynamic properties and integration in solar reactors are still few and limited to specific compositional windows–mainly lanthanum-based perovskites–and small-scale laboratory conditions (Lu et al., 2019; Haeussler et al., 2018).

In addition to the reduction extent of the material, another factor limiting the efficiencies of experimental two-step thermochemical cycles is the large amount of heat dispersed between reduction and oxidation, when a temperature swing is implemented between the two steps as more commonly adopted so far. This amount of sensible heat is associated both to the solid phase (redox material and reactor components) and to the gas phase (sweep gas and oxidizing fluid). In order to increase the overall performance, it becomes essential to modify the standard design of reactors by integrating heat recovery techniques for both solid and gas sensible heat. It was reported that the implementation of these techniques in solar thermochemical cycles could rise their efficiencies up to 20%, making them more competitive for commercial scale applications (Wei et al., 2023). An example of solid-phase heat recovery concept is provided by the Reactor Train System (RTS) developed by Patankar et al. (2022), where multiple reactors are cycled between the two steps in order to pre-heat the ones entering the reduction zone by using the ones exiting it in the opposite direction–a form of counterflow radiative heat recovery. A solution for gas-phase heat recovery is proposed by Bader et al. (2015), where two concentric tubes are adopted in order to pre-heat the inlet fluid with the outlet fluid.

In this context, numerical modeling has a key role in guiding the engineering process, allowing the simulation of complex reactors and evaluating the optimal solutions in terms of design, materials to be used, and operational regimes, thereby limiting the need for expensive experimental procedures (Brendelberger et al., 2020). The main challenge is that, in such systems, different heat and mass transfer processes are involved, requiring a complex multiphysics model to couple the micro- and macro-scale (Wang et al., 2022). More specifically, the main physical phenomena that should be integrated in the process are the fluid flow inside the reactor, the chemical reaction between the fluid and the solid (redox material) phases, and the heat exchange (including conduction, convection, and radiation).

Numerous reviews have been published over the years on two-step thermochemical cycles. Most recent contributions include the works from Tran et al. (2024), Wei et al. (2023), and Guo et al. (2024), where the main advances in terms of redox material, reactors design, and operation of the system are collected. In addition, Lidor and Bulfin (2024) lately proposed a critical analysis of the main limitations of real reactors and their future scale-up, highlighting the requirements to improve the power density of these systems. Reviews focusing on the modeling side of this topic are much more limited and not updated. The work developed by Lipiński et al. (2021) provides a complete analysis of the main processes for high-temperature solar thermal applications, but limited to the heat transfer modeling. To the best of the authors' knowledge, the work published in 2017 by Wheeler et al. (2017) represents the only example of panoramic review on the modeling of solar thermochemical reactors, with a general description of the main modeling approaches for different types of reactors (*i.e.*, fluidized and stationary), as well as of reactive materials properties evaluation.

The lack of updated reviews with a focus on the multiphysics modeling of different types of solar reactors for thermochemical fuel production is addressed in this paper. Specifically, this work aims to provide a compact overview of the main continuum-scale models developed for non-volatile and non-stoichiometric two-step thermochemical cycles, currently representing the most explored approach, highlighting the differences adopted in terms of reactor design, morphology of the redox material, and mathematical approaches for the numerical simulation.

The work is organized as follows. In Section 2, the methodology applied for conducting the literature review, and the selection criteria of the analyzed works, are presented. Section 3 reports a comprehensive discussion on solar thermochemical reactor modeling, and the most relevant works published on this subject. A particular focus was given to the different types of reactors considered in these models (Section 3.1) and to the most common modeling approaches in terms of heat and mass transfer, chemical reaction, and radiation (Section 3.2). Finally, a critical discussion of the main outcomes from the literature review is presented in Section 4.

## 2 Methodology

The literature review strategy is schematized in Figure 2 and detailed below in this section.

Preliminary research was carried out on the search engine Scopus (Scopus, 2025) according to the keywords "solar thermochemical reactor", "solar thermochemical cycle", "model", and "simulation", excluding the review articles and the publications not in English. The research provided 819 results, from which publications not related to the topic of the paper (*i.e.*, solar thermochemical cycles for methane or methanol reforming, calcium looping, thermochemical energy storage) and publications not related to

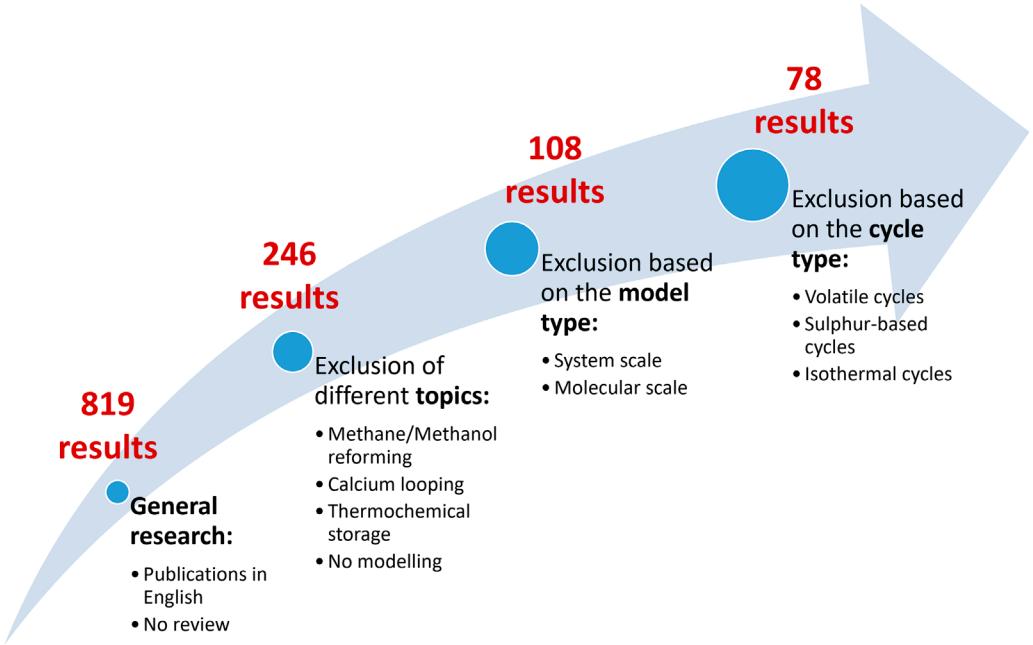


FIGURE 2
Sources selection strategy for the literature review. General research was carried out on the search engine Scopus according to the keywords "solar thermochemical reactor", "solar thermochemical cycle", "model", and "simulation", excluding the review articles and publications not in English. The complete search syntax that was used to get the first 819 results is the following: [solar AND thermochemical AND (cycle OR reactor)] AND (model OR simulation).

modeling were removed. In this way, the total amount of results was limited to 246 studies.

An important feature associated to the modeling of thermochemical cycles lies in the large span of their temporal and spatial scales. The time scale spans from the seasonal variation of solar irradiation, down to the very fast chemical kinetics. Similarly, from a spatial perspective, the process encompasses the larger scale of the plant (*e.g.,* solar radiation collection and concentration systems, reactor scale), as well as the micrometer/nanometer or molecular scale of the materials that participate to the chemical reactions. From a mathematical perspective, different approaches can be defined depending on the temporal or spatial scale considered, as well as on the aim of the analysis. A general classification of the different categories of models evaluated in this first preliminary analysis is provided in Figure 3.

Models focusing on the material scale typically aim to describe either the thermodynamics of the chemical reaction [*e.g.*, with examples on ceria (Scheffe and Steinfeld, 2012) and perovskites (Scheffe et al., 2013; Lou et al., 2024)], its kinetics [*e.g.*, with examples on ceria (Arifin and Weimer, 2018), LSM-based perovskites (Pan et al., 2024), and hercynites (Al-Shankiti et al., 2020)], or the effective thermal and transport properties of the redox materials (Xu and Lin, 2023; Ackermann et al., 2014). Models focusing on the reactor scale aim to provide a numerical representation in which the heat and mass transport processes involved are described on a length scale comparable to the reactor scale. This continuum approach avoids the need to solve local boundaries between solid and gaseous phases on a discrete scale, thereby reducing the simulation complexity and the computational costs. The governing equations at the continuum scale result from a homogenization process, in which the physical processes at a small scale are rigorously averaged to retain macroscopic behaviors (Wheeler et al., 2017). In this way, the reactive medium is approximated by considering it as two homogeneous and continuous phases–gas and solid–with effective transport and thermal properties determined experimentally or through numerical simulations (Perraudin and Haussener, 2017). Following this approach, models focusing on particle flow in the reactor (Richter et al., 2025), radiative heat transfer (Villafán-Vidales et al., 2012), and control strategies (Oberkirsch et al., 2022) were proposed in literature. In addition, multiphysics modeling allows to treat the different physical phenomena characterizing the redox cycle (namely: fluid flow, heat and mass transfer, and chemical reactions) by coupling them together. Finally, models considering the whole system (*e.g.*, including the solar concentrating system, the solar reactor, and auxiliary components) are usually developed to provide a generalized description of the cycle without a detailed analysis on the physical phenomena. Examples in this category are represented by dynamic simulation models for long term evaluation of the process (Barone et al., 2023; de la Calle and Bayon, 2019), thermodynamic models for energy, exergy, and performance analysis (Muhich et al., 2018; Long et al., 2024; Yang et al., 2021), or techno-economic models (Onigbajumo et al., 2022).

The presented review is focused specifically on multiphysics modeling, and for this reason, only this category of models is analyzed and presented in this work. By excluding material- and system-scale models, the total amount of papers was narrowed down to 108 results.

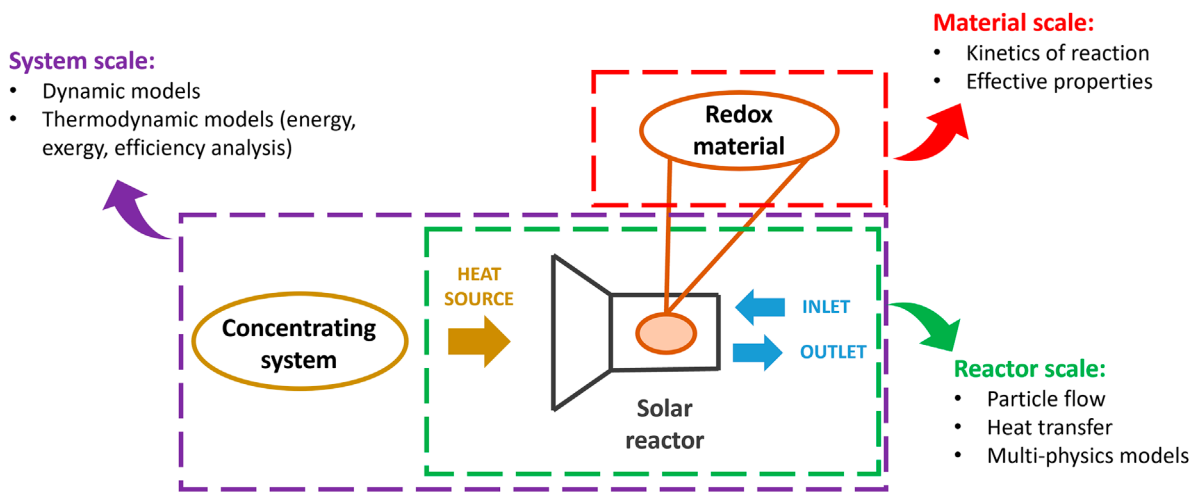


FIGURE 3
Classification of models for solar thermochemical cycles based on their spatial scale.

In addition, since the focus of the review is on the analysis of multiphysics models related to non-volatile and non-stoichiometric cycles, the studies focusing on alternative approaches were not included in this study–see the general classification proposed in Figure 1. Consequently, the papers regarding volatile cycles [*e.g.*, ZnO (Mohite and Reddy, 2023)], non-volatile stoichiometric cycles [*e.g.*, $Fe_3O_4$ (Guene Lougou et al., 2017a), $Co_3O_4$ (Kopping et al., 2019), $Mn_3O_4$ (Alonso and Romero, 2015; Wang et al., 2020)], 3-steps cycles [*e.g.*, S-I (Corgnale et al., 2019)], 4-step cycles [*e.g.*, Cu-Cl (Xu and Wiesner, 2012)], and hybrid cycles [*e.g.*, HyS (Bayer Botero et al., 2016)], were excluded from the analysis.

In conclusion, the described selection strategy led to a total of 78 results analyzed in the literature review. The main different types of solar reactors and the different modeling approaches provided in these studies are discussed in detail in the following. The results of the preliminary analysis described in the current section, in terms of number of publications in the last 15 years per type of cycle (Figure 4a) and type of model (Figure 4b), confirm the growing interest in non-volatile two-step thermochemical cycles under different perspectives.

# 3 Multiphysics modeling of solar thermochemical cycles

Solar thermochemical reaction systems, and specifically two-step solar thermochemical cycles, typically involve solid-gas chemical reactions occurring at the interface between a solid reactive phase and a gaseous phase, usually at high temperatures (in the range 800 °C–1,500 °C) and under temperature and pressure swing conditions. The main challenge in the modeling of such systems is their multiphysical nature, since heat transfer from different mechanisms, as well as momentum and mass transfer of the different reactive species, need to be considered together with chemistry and must be coupled effectively.

Concerning the process operation, depending on the morphology of the reactive material integrated in the reactor, different regimes can be defined, namely: a dilute fluidized regime, a dense fluidized regime, or a stationary regime (Wheeler et al., 2017). The dilute fluidized regime involves a redox material composed of suspended or fluidized particles that occupy a small fraction of the total volume, and the interactions between the particles can be neglected. The dense fluidized regime refers to a case in which the reacting particles occupy a larger fraction of the reactor volume, and their interactions are more significant. Finally, in the stationary regime, the redox material is fixed in the reactor (*i.e.*, porous structure or packed bed of particles) (Wheeler et al., 2017). Thanks to their increased easiness in handling the reactive material and separating the gaseous products, the systems based either on a dense fluidized regime or on a stationary regime are the most developed. For this reason, the present study focuses on multiphysics models within these two categories.

## 3.1 Solar reactor modeling

Each model available in the literature describes a reactor device with different features in terms of design and working principle, as well as in terms of redox material composition, shaping, and morphology. A straightforward classification of solar thermochemical reactors is done based on how the solar radiation is transferred to the reactive redox material, dividing the designs in either directly or indirectly irradiated. In the first case, the reactive redox material is directly exposed to the external radiative source, whereas in the second case an intermediate surface absorbs the radiative heat and re-emits it towards the reactive material inside the reactor. Directly irradiated reactors are the most developed solution up to date thanks to their simple structure, low thermal inertia, and possibility to reach higher temperatures (Wang et al., 2024). On the other hand, the indirectly irradiated design can guarantee lower optical losses (Huang and Lin, 2021). For specific configurations, the

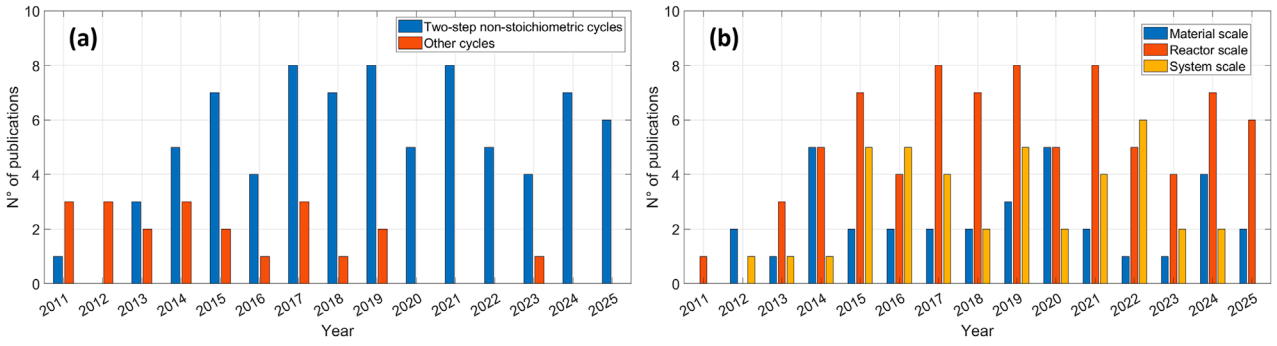


FIGURE 4
Number of publications in the last 15 years. **(a)** Multiphysics models sorted by type of cycle considered: two-step nonstoichiometric cycles and other cycles (including three-steps, four-steps, hybrid, and volatile cycles) are reported. **(b)** Two-step nonstoichiometric cycles models sorted by the modeling scale considered (i.e., redox material, reactor, and system).

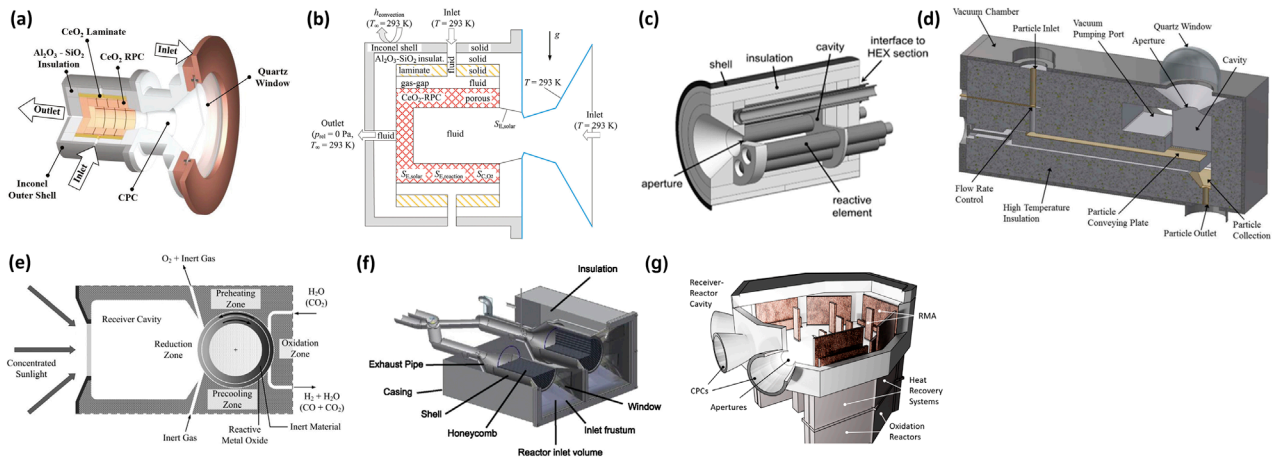


FIGURE 5
Different types of solar reactors from the literature. **(a, b)** Cavity-type, directly irradiated reactor (Furler and Steinfeld, 2015, licesend under CC BY-NC-ND 4.0); **(c)** Tubular reactor filled with a bed of reactive particles (Bader et al., 2015, © 2015 by ASME); **(d)** Moving particles reactor (Singh et al., 2017, © 2017 Elsevier Ltd.); **(e)** Rotating reactor (Lapp and Lipiński, 2014, © 2014 by ASME); **(f)** Honeycomb reactor (Lange et al., 2015, © 2015 Hydrogen Energy Publications, LLC.); **(g)** Receiver-reactor cavity system with multiple mobile redox units (R2Mx) (Vega Puga et al., 2024, © 2024 by ASME).

indirectly irradiated design can lead to an improvement of the view factors by placing the redox material closer to the emitting surface, enabling a more uniform heat flux, and avoiding point-focused radiation (Scott et al., 2024).

One of the most common types of reactors in modeling studies is the abovementioned cavity-type reactor, in which the radiative heat source is provided through an aperture enclosed by a window. Alternative designs are represented by tubular, membrane, or moving reactors. A collected representation of the main types of reactors proposed up to date, modelled in the literature and described in the following sections, is provided in Figure 5.

Concerning the redox material, different alternatives were proposed, regarding both the composition and its morphology. Nonstoichiometric ceria ($CeO_2$) has been by far the most exploited material up to date, thanks to its crystallographic stability, fast kinetics, cyclic durability, and abundance (Schäppi et al., 2022). Promising alternatives are represented by ferrites or perovskites (Wei et al., 2023). Regarding the morphology of the redox material, a reticulated porous ceramics (RPC) structure is generally preferred compared to other solutions such as fluidized beds (Bellan et al., 2019) or moving particles (Li et al., 2020; Falter and Pitz-Paal, 2018), since the material remains fixed in space. As a consequence, particle transport between reaction steps is bypassed and no constraints on the minimum gas flow rate are needed during the operation of the system (Haeussler et al., 2020b). A classification of the multiphysics models considered in this work according to the reactor type

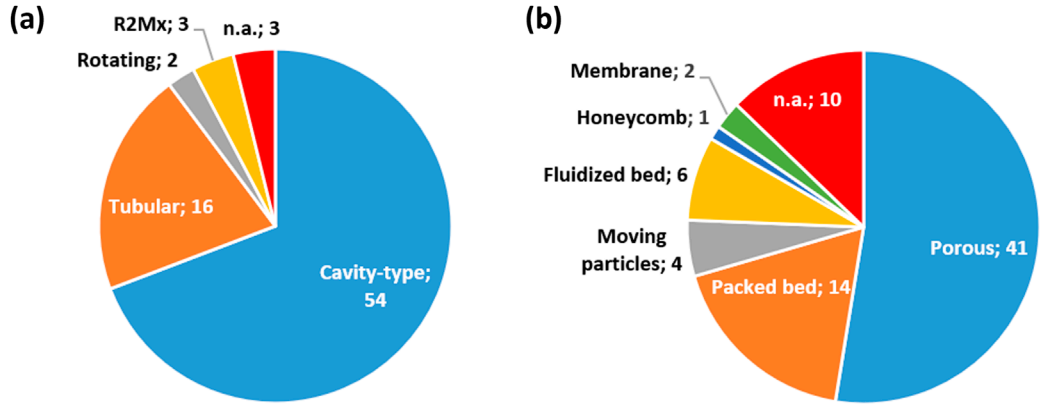


FIGURE 6
Multiphysics models considered in this review sorted by **(a)** reactor type and **(b)** morphology of the redox material. **(b)** In the term "porous" refers to a reticulated porous structure with single-scale or dual-scale porosity. The share "n.a." includes models where the reactor type or the redox material morphology are not specified.

and morphology of the redox material is provided in Figure 6. A summary of the models analyzed in this study and discussed in the following sections, together with their main features in terms of design, redox material, and modeling figures, is reported in Table 1.

### 3.1.1 Reactor design

As indicated above, the main distinction of different types of reactors is between directly or indirectly irradiated reactors. In addition to the radiation transfer mechanism, other design choices characterize reactors for thermochemical fuel production, such as the choice of materials for the reactive chamber, the concentration technology, or the integration of heat recovery techniques. In this section, various models are introduced together with their main features in terms of design choices and aim of the analysis.

#### 3.1.1.1 Cavity-type directly irradiated reactors

The cavity-type directly irradiated configuration represents the reactor class that was most explored throughout the literature so far, and numerous modeling works were developed to analyze the reactor performance considering different designs, morphologies of the redox material, and operating conditions (Figures 5a,b).

Regarding the design choices, different positions of inlet and outlet nozzles were evaluated by Zhang and Smith (2019), displaying a small effect on the temperature distribution and indicating the configuration with fluid entering and exiting from the top of the reactor as the more favorable option. Similarly, Furler and Steinfeld (2015) considered different configurations in terms of number and location of the inlet nozzles to prevent gas recirculation at the reactor front. The same study also proposed the implementation of a secondary concentrator to enhance the temperature distribution in the reactive medium, enabling a more uniform radiation absorption and preventing local hot spots. Guene Lougou et al. (2018a), Guene Lougou et al. (2023) evaluated the effect of the internal surface properties of the cavity on the thermal performance of the reactor. In particular, the emissivity of the internal walls significantly affects the temperature distribution for both the fluid and the solid phase and the radiative heat transfer, while the emissivity of the glass window has a lower effect on the solid phase due to the distance between the two components. The analysis of the radiative flux distribution over different geometries of the cavity and positions of the focal point was presented by Sharma et al. (2023). Lidor et al. (2021) considered the integration of a gas-phase heat recovery system and the operation over a complete day, indicating an increased overall efficiency even in the case with the simplest configuration of heat recovery system considered in the study (heat exchanger at the reactor inlet/outlet). The implementation of a cut-off wavelength coating was considered by Ma et al. (2024), with the aim of limiting the re-radiation losses from the internal reactor surfaces. The results with a cut off of wavelength larger than 1 μm indicated benefits both in terms of average temperature (from 1,510.77 °C to 1,634.87 °C) and thermal efficiency (from 11.65% to 13.51%).

For what concerns the redox material, it is of central interest to optimize its morphology in order to maximize the surface area available for the chemical reaction, as well as to promote a more uniform temperature field. In this context, several studies evaluated the impact of considering various reticulated porous structures (specifically, parameters such as single-scale porosity, mean pore diameter, porous medium thickness, or mass loading of redox material) on oxygen and/or hydrogen production rates (Keene et al., 2014; Lidor et al., 2021), solar-to-fuel efficiency (Zoller et al., 2019), or thermal performance of the system (Villafán-Vidales et al., 2011; Guene Lougou et al., 2018a; Pan et al., 2018). Moving the attention to beds of reactive particles, similar studies were performed in order to define the effect on temperature distribution and performance of cavity-type reactors for varying particle size (Zhang and Smith, 2021; Sedighi et al., 2021), packing arrangements (Darfilal, 2020), thickness of the bed (Zhang and Smith, 2019), or redox mass loading (Bellan et al., 2019). Lange et al. (2015) considered the effect of different redox mass loading in a honeycomb structure. Guene Lougou et al. (2018b) evaluated the thermal performance of various foam-type porous structures based on nickel ferrite

TABLE 1 Summary of the reactor models reported in the literature, organized according to the reactor type, and ordered following the year of publication.

| Study | Year | Software | Geometry | Directly/Indirectly irradiated | Reactor design | Redox material | Morphology | Nominal power [kW] | Fluid flow | Heat transfer | Radiative heat transfer | Reduction | Oxidation | Kinetics |
|---|---|---|---|---|---|---|---|---|---|---|---|---|---|---|
| **Cavity type reactors** | | | | | | | | | | | | | | |
| Villafán-Vidales et al. (2011) | 2011 | ANSYS Fluent® | 2D | Directly | Cavity type | Nickel ferrite | Porous | 1 | ✓ | ✓ | ✓ | ✓ | ✓ | ✓ |
| Lanchi et al. (2013) | 2013 | COMSOL Multiphysics® *(Software version n.a.)* | 2D | Indirectly | Cavity type | Manganese ferrite | Packed bed | 1 | ✓ | ✓ | ✓ | | | |
| Bellan et al. (2013) | 2013 | COMSOL Multiphysics® 4.2 | 3D | Directly | Cavity type | — | — | 2.1 | ✓ | ✓ | ✓ | | | |
| Keene et al. (2014) | 2014 | FORTRAN code | 1D | Directly | Cavity type | Ceria | Porous | — | ✓ | ✓ | ✓ | ✓ | | ✓ |
| Bellan et al. (2014a) | 2014 | COMSOL Multiphysics® 4.3 | 3D | Directly | Cavity type | — | — | 2.1 | ✓ | ✓ | ✓ | | | |
| Bellan et al. (2014b) | 2014 | COMSOL Multiphysics® 4.2 | 3D | Directly | Cavity type | — | — | — | ✓ | ✓ | ✓ | | | |
| Oles and Jackson (2015) | 2015 | MATLAB *(Software version n.a.)* | 3D | Directly | Cavity type | Ceria | Moving particles | — | ✓ | ✓ | ✓ | ✓ | | ✓ |
| Furler and Steinfeld (2015) | 2015 | ANSYS CFX® 14.0 + VEGAS code | 3D | Directly | Cavity type | Ceria | Porous | 4 | ✓ | ✓ | ✓ | ✓ | | ✓ |
| Lange et al. (2015) | 2015 | Aspen custom modeler | 2D | Directly | Cavity type | Nickel ferrite | Honeycomb | — | ✓ | ✓ | ✓ | | | |
| Ma et al. (2015) | 2015 | ANSYS® 14.5 | 3D | Indirectly | Cavity type | — | — | — | ✓ | ✓ | ✓ | | | |

(Continued on the following page)



10.3389/fenrg.2025.1671615

TABLE 1 (*Continued*) Summary of the reactor models reported in the literature, organized according to the reactor type, and ordered following the year of publication.

| Study | Year | Software | Geometry | Directly/Indirectly irradiated | Reactor design | Redox material | Morphology | Nominal power [kW] | Fluid flow | Heat transfer | Radiative heat transfer | Reduction | Oxidation | Kinetics |
|---|---|---|---|---|---|---|---|---|---|---|---|---|---|---|
| Singh et al. (2017) | 2017 | *software n.a.* | 3D | Directly | Cavity type | — | Moving particles | — | ✓ | ✓ | ✓ | | | |
| Ackermann et al. (2017) | 2017 | ANSYS academic Research® 15.0 | 1D | Directly | Cavity type | Ceria | Dual-scale porosity | — | ✓ | ✓ | ✓ | ✓ | | |
| Grobbel et al. (2017) | 2017 | ANSYS workbench *(Software version n.a.)* | 2D | Directly | Cavity type | — | Packed bed | 1.84* | | ✓ | ✓ | | | |
| Guene Lougou et al. (2017b) | 2017 | OpenFOAM 2.4.0 | 2D | Directly | Cavity type | — | — | — | ✓ | ✓ | ✓ | | | |
| Guene Lougou et al. (2017c) | 2017 | OpenFOAM 2.4.0 | 3D | Directly | Cavity type | — | — | — | ✓ | ✓ | ✓ | | | |
| Bellan et al. (2018a) | 2018 | ANSYS Fluent® *(Software version n.a.)* | 3D | Directly | Cavity type | — | Fluidized bed | 3.2* | ✓ | ✓ | ✓ | | | |
| Bellan et al. (2018b) | 2018 | ANSYS Fluent® 17.0 | 3D | Directly | Cavity type | — | Fluidized bed | 3.2* | ✓ | ✓ | ✓ | | | |
| Guene Lougou et al. (2018a) | 2018 | COMSOL Multiphysics® 5.3 | 3D | Directly | Cavity type | Nickel ferrite | Porous | — | ✓ | ✓ | ✓ | | | |
| Guene Lougou et al. (2018b) | 2018 | COMSOL Multiphysics® 5.3 | 3D | Directly | Cavity type | Nickel ferrite | Porous | — | ✓ | ✓ | ✓ | | | |
| Zhang et al. (2018) | 2018 | ANSYS Fluent® *(Software version n.a.)* | 3D | Directly | Cavity type | — | Porous | — | ✓ | ✓ | ✓ | | | |
| Abedini Najafabadi and Ozalp (2018) | 2018 | *software n.a.* | 2D | Directly | Cavity type | — | — | 7 | ✓ | ✓ | ✓ | | | |

(Continued on the following page)



10.3389/fenrg.2025.1671615

TABLE 1 (*Continued*) Summary of the reactor models reported in the literature, organized according to the reactor type, and ordered following the year of publication.

| Study | Year | Software | Geometry | Directly/Indirectly irradiated | Reactor design | Redox material | Morphology | Nominal power [kW] | Fluid flow | Heat transfer | Radiative heat transfer | Reduction | Oxidation | Kinetics |
|---|---|---|---|---|---|---|---|---|---|---|---|---|---|---|
| Zhang and Smith (2019) | 2019 | STAR-CCM+ 12.6 | 3D | Directly | Cavity type | Ceria | Packed bed | — | ✓ | ✓ | ✓ | ✓ | | |
| Zoller et al. (2019) | 2019 | ANSYS CFX® 17.0 | 2D axial-symmetric | Directly | Cavity type | Ceria | Dual-scale porosity | 50 | | ✓ | ✓ | ✓ | | |
| Kyrimis et al. (2019) | 2019 | ANSYS CFX® 17.1 | 3D | Directly | Cavity type | Ceria | Dual-scale porosity | 300–3,000 | ✓ | ✓ | ✓ | ✓ | | |
| Bellan et al. (2019) | 2019 | ANSYS Fluent® 18.0 | 3D | Directly | Cavity type | — | Fluidized bed | 30 | ✓ | ✓ | ✓ | | | |
| Pan et al. (2018) | 2019 | COMSOL Multiphysics® 5.3 | 3D | Directly | Cavity type | — | Porous | — | ✓ | ✓ | ✓ | | | |
| Brendelberger et al. (2019a) | 2019 | Python 3.6 | 1D | Directly | Cavity type | Ceria | Porous | 300 | | ✓ | ✓ | ✓ | ✓ | |
| Brendelberger et al. (2020) | 2020 | Python 3.6 | 1D | Directly | Cavity type | Ceria | Porous | 433 | | ✓ | ✓ | ✓ | ✓ | |
| Zhang et al. (2020) | 2020 | ANSYS Mechanical® 16.0 + ANSYS mechanical APDL® 16.0 | 3D | Directly | Cavity type | — | — | 6–15* | ✓ | ✓ | ✓ | | | |
| Getahun Dessi et al. (2020) | 2020 | COMSOL Multiphysics® 5.3 | 2D | Directly | Cavity type | — | — | — | ✓ | ✓ | ✓ | | | |
| Guene Lougou et al. (2020) | 2020 | COMSOL Multiphysics® 5.4 | 3D | Directly | Cavity type | Nickel ferrite | Porous | — | ✓ | ✓ | ✓ | | | |
| Shuai et al. (2021) | 2021 | COMSOL Multiphysics® 5.3 | 3D | Directly | Cavity type | Nickel ferrite | Porous | 10* | ✓ | ✓ | ✓ | | | |

(Continued on the following page)



10.3389/fenrg.2025.1671615

TABLE 1 (*Continued*) Summary of the reactor models reported in the literature, organized according to the reactor type, and ordered following the year of publication.

| Study | Year | Software | Geometry | Directly/Indirectly irradiated | Reactor design | Redox material | Morphology | Nominal power [kW] | Fluid flow | Heat transfer | Radiative heat transfer | Reduction | Oxidation | Kinetics |
|---|---|---|---|---|---|---|---|---|---|---|---|---|---|---|
| Huang and Lin (2021) | 2021 | COMSOL Multiphysics® 5.6 | 3D | Both | Cavity type | — | Porous | 1–7* | ✓ | ✓ | ✓ | | | |
| Wang et al. (2021) | 2021 | ANSYS Fluent® 18.2 + FORTRAN code | 3D | Indirectly | Cavity type | Manganese ferrite | Packed bed | 10.6 | ✓ | ✓ | ✓ | ✓ | ✓ | ✓ |
| Lidor et al. (2021) | 2021 | MONROE code | 1D | Directly | Cavity type | Ceria | Porous | — | ✓ | ✓ | ✓ | ✓ | ✓ | |
| Zhang and Smith (2021) | 2021 | STAR-CCM+ 12.02 | 3D | Directly | Cavity type | Ceria | Packed bed | 4.5* | ✓ | ✓ | ✓ | ✓ | | |
| Shu et al. (2021) | 2021 | COMSOL Multiphysics® 5.3 | 3D | Directly | Cavity type | Nickel ferrite – $ZrO_2$ | Porous | 4.9* | ✓ | ✓ | ✓ | ✓ | ✓ | ✓ |
| Sedighi et al. (2021) | 2021 | ANSYS Fluent® 2019 + TracePro | 3D | Directly | Cavity type | — | Packed bed | 72* | ✓ | ✓ | ✓ | | | |
| Huang and Lin (2022) | 2022 | COMSOL Multiphysics® 6.0 | 2D axial-symmetric | Indirectly | Cavity type | Ceria | Porous | — | ✓ | ✓ | ✓ | ✓ | ✓ | ✓ |
| Wang et al. (2022) | 2022 | *software n.a.* | 2D | Directly | Cavity type | Ceria | Porous | — | ✓ | ✓ | ✓ | ✓ | ✓ | ✓ |
| Dai and Haussener (2022) | 2022 | COMSOL Multiphysics® 5.3 | 1D | Directly | Cavity type | Ceria | Porous | — | ✓ | ✓ | ✓ | ✓ | ✓ | ✓ |
| Bellan et al. (2022) | 2022 | ANSYS Fluent® 17.0 | 3D | Directly | Cavity type | — | Fluidized bed | 30 | ✓ | ✓ | ✓ | | | |

(Continued on the following page)



10.3389/fenrg.2025.1671615

TABLE 1 (*Continued*) Summary of the reactor models reported in the literature, organized according to the reactor type, and ordered following the year of publication.

| Study | Year | Software | Geometry | Directly/Indirectly irradiated | Reactor design | Redox material | Morphology | Nominal power [kW] | Fluid flow | Heat transfer | Radiative heat transfer | Reduction | Oxidation | Kinetics |
|---|---|---|---|---|---|---|---|---|---|---|---|---|---|---|
| Sharma et al. (2023) | 2023 | ANSYS Fluent® 16.0 + SolTrace | 3D | Directly | Cavity type | Ceria | Porous | — | ✓ | ✓ | ✓ | ✓ | | |
| Guene Lougou et al. (2023) | 2023 | *software n.a.* | 3D | Directly | Cavity type | $Co_3O_4$-$CuFe_2O_4$ | Porous | 4.5* | ✓ | ✓ | ✓ | ✓ | ✓ | ✓ |
| Menz et al. (2023) | 2023 | MATLAB® simscape 2020b | 3D | Directly | Cavity type | Ceria | Porous | 250 | | ✓ | ✓ | ✓ | | ✓ |
| Scott et al. (2024) | 2024 | COMSOL Multiphysics® 6.2 | 2D axial-symmetric | Indirectly | Cavity type | Ceria | Dual-scale porosity | — | | ✓ | ✓ | ✓ | | |
| Ma et al. (2024) | 2024 | *software n.a.* | 3D | Directly | Cavity type | Ceria-$ZrO_2$ | Porous | 7.46* | ✓ | ✓ | | ✓ | | ✓ |
| Cai et al. (2024) | 2024 | COMSOL Multiphysics® 6.1 | 3D | Directly | Cavity type | Ceria | Porous | — | ✓ | ✓ | ✓ | | | |
| Orsini et al. (2024) | 2024 | COMSOL Multiphysics® 6.2 | 1D | Directly | Cavity type | Ceria | Porous | — | ✓ | ✓ | ✓ | ✓ | ✓ | ✓ |
| Lampe and Menz (2024) | 2024 | MATLAB® simscape *(Software version n.a.)* | 3D | Directly | Cavity type | Ceria | Porous | 250 | ✓ | ✓ | ✓ | ✓ | ✓ | ✓ |
| Rojas et al. (2025) | 2025 | *software n.a.* | 1D | Directly | Cavity type | Ceria | Porous | 3 | | ✓ | | ✓ | ✓ | ✓ |
| Wang et al. (2025) | 2025 | COMSOL Multiphysics® *(Software version n.a.)* | 3D | Directly | Cavity type | Ceria | Porous | — | ✓ | | | ✓ | | |

(Continued on the following page)



10.3389/fenrg.2025.1671615

TABLE 1 (*Continued*) Summary of the reactor models reported in the literature, organized according to the reactor type, and ordered following the year of publication.

| Study | Year | Software | Geometry | Directly/Indirectly irradiated | Reactor design | Redox material | Morphology | Nominal power [kW] | Fluid flow | Heat transfer | Radiative heat transfer | Reduction | Oxidation | Kinetics |
|---|---|---|---|---|---|---|---|---|---|---|---|---|---|---|
| Lampe et al. (2025a) | 2025 | MATLAB® simscape *(Software version n.a.)* | 3D | Directly | Cavity type | Ceria | Porous | 250 | ✓ | ✓ | ✓ | ✓ | ✓ | ✓ |
| Lampe et al. (2025b) | 2025 | MATLAB® simscape 2021a | 3D | Directly | Cavity type | Ceria | Porous | 250 | ✓ | ✓ | ✓ | ✓ | ✓ | ✓ |
| **Tubular reactors** | | | | | | | | | | | | | | |
| Martinek et al. (2014) | 2014 | ANSYS Fluent® 14.0 | 3D | Indirectly | Tubular | Hercynite | Packed bed | 4 | ✓ | ✓ | ✓ | ✓ | ✓ | ✓ |
| Bader et al. (2015) | 2015 | FORTRAN code | 3D | Indirectly | Tubular | Ceria | Packed bed | 3 | ✓ | ✓ | ✓ | ✓ | ✓ | |
| Yuan et al. (2016) | 2015 | *software n.a.* | 1D | Indirectly | Tubular | Ceria | Packed bed | 1 | | ✓ | | ✓ | ✓ | ✓ |
| Bala Chandran et al. (2015) | 2015 | ANSYS Fluent® 15.0 | 2D axial-symmetric | Indirectly | Tubular | Ceria | Packed bed | 3* | ✓ | ✓ | ✓ | | | |
| Hathaway et al. (2015) | 2016 | ANSYS Fluent® 15.0 | 2D axial-symmetric | Indirectly | Tubular | Ceria | Packed bed | 4 | ✓ | ✓ | ✓ | ✓ | ✓ | |
| Bala Chandran and Davidson (2016) | 2016 | ANSYS Fluent® 15.0 | 3D | Indirectly | Tubular | Ceria | Packed bed | 4 | ✓ | ✓ | ✓ | ✓ | ✓ | |
| Li et al. (2016) | 2016 | *software n.a.* | 3D | Indirectly | Tubular | Ceria | Packed bed | 10 | | ✓ | ✓ | ✓ | | |
| Valle-Hernández et al. (2017) | 2016 | *software n.a.* | 3D | Indirectly | Tubular | Ceria | Porous | — | ✓ | ✓ | ✓ | ✓ | | ✓ |

(Continued on the following page)



10.3389/fenrg.2025.1671615

TABLE 1 (*Continued*) Summary of the reactor models reported in the literature, organized according to the reactor type, and ordered following the year of publication.

| Study | Year | Software | Geometry | Directly/Indirectly irradiated | Reactor design | Redox material | Morphology | Nominal power [kW] | Fluid flow | Heat transfer | Radiative heat transfer | Reduction | Oxidation | Kinetics |
|---|---|---|---|---|---|---|---|---|---|---|---|---|---|---|
| Valadés-P et al. (2017) | 2017 | *software n.a.* | 3D | Indirectly | Tubular | Ceria | Fluidized bed | 25 | ✓ | ✓ | ✓ | | | |
| Valades-Pelayo et al. (2017) | 2017 | *software n.a.* | 3D | Indirectly | Tubular | Ceria | Fluidized bed | — | ✓ | ✓ | ✓ | ✓ | | ✓ |
| Valle-Hernández et al. (2017) | 2017 | *software n.a.* | 3D | Indirectly | Tubular | Ceria | Porous | — | ✓ | ✓ | ✓ | | ✓ | ✓ |
| Falter and Pitz-Paal (2018) | 2018 | MATLAB® *(Software version n.a.)* | 3D | Indirectly | Tubular | Ceria | Moving particles | 4 | | ✓ | ✓ | | | |
| Tapia et al. (2019) | 2019 | ANSYS CFX® 14.0 | 3D | Indirectly | Tubular | Ferrite | Packed bed | 100 | ✓ | ✓ | ✓ | | | |
| Li et al. (2020) | 2020 | ANSYS Fluent® 17.1 | 3D | Indirectly | Tubular | Ceria | Moving particles | — | ✓ | | | ✓ | | ✓ |
| Pan et al. (2020) | 2021 | COMSOL Multiphysics® *(Software version n.a.)* | 2D axial-symmetric | — | Tubular | Ceria | Membrane | — | ✓ | ✓ | | ✓ | ✓ | ✓ |
| Wei et al. (2024) | 2024 | ANSYS Fluent® 16.0 | 2D | Directly | Tubular | Ceria | Membrane | — | ✓ | ✓ | ✓ | | ✓ | |
| **Rotating reactors** | | | | | | | | | | | | | | |
| Lapp et al. (2013) | 2013 | FORTRAN code | 2D | Directly | Rotating | Ceria | Porous | 3 | | ✓ | ✓ | | | |
| Lapp and Lipiński (2014) | 2014 | FORTRAN code | 3D | Directly | Rotating | Ceria | Porous | 3 | | ✓ | ✓ | ✓ | ✓ | |

(Continued on the following page)



10.3389/fenrg.2025.1671615

TABLE 1 (*Continued*) Summary of the reactor models reported in the literature, organized according to the reactor type, and ordered following the year of publication.

| Study | Year | Software | Geometry | Directly/Indirectly irradiated | Reactor design | Redox material | Morphology | Nominal power [kW] | Fluid flow | Heat transfer | Radiative heat transfer | Reduction | Oxidation | Kinetics |
|---|---|---|---|---|---|---|---|---|---|---|---|---|---|---|
| **R2Mx reactors** | | | | | | | | | | | | | | |
| Brendelberger et al. (2022) | 2022 | Python 3.7 | 1D | Indirectly | R2Mx | Ceria | Porous | 250 | | ✓ | ✓ | ✓ | | |
| Vega Puga et al. (2024) | 2023 | ANSYS Mechanical® *(Software version n.a.)* | 2D axial-symmetric | — | R2Mx | Ceria | Dual-scale porosity | — | | ✓ | ✓ | ✓ | ✓ | |
| Brendelberger (2024) | 2024 | Python 3.11 | 1D | Indirectly | R2Mx | Ceria | Dual-scale porosity | $13.7{\cdot}10^3$ | | ✓ | ✓ | ✓ | | |
| **Others** | | | | | | | | | | | | | | |
| Brendelberger et al. (2019b) | 2019 | Python 3.6 | 0D | — | — | Ceria (splitting material) + $SrFeO_3$ (thermochemical pumping material) | — | — | | | | ✓ | | |
| Zhao et al. (2025a) | 2025 | COMSOL Multiphysics® 6.0 | 2D axial-symmetric | — | — | Ceria, $Zr_{0.15}Ce_{0.85}O_2$, $La_{0.6}Ca_{0.4}Mn_{0.6}Al_{0.4}O_3$, $La_{0.8}Sr_{0.2}MnO_3$ | Dual-scale porosity | 0.04–0.1 | ✓ | ✓ | ✓ | ✓ | ✓ | |
| Zhao et al. (2025b) | 2025 | COMSOL Multiphysics® 6.0 | 2D axial-symmetric | — | — | Ceria, $La_{0.6}Ca_{0.4}Mn_{0.6}Al_{0.4}O_3$, $CaTi_{0.5}Mn_{0.5}O_3$, $(La_{1/6}Pr_{1/6}Nd_{1/6}Gd_{1/6}Sr_{1/6}Ba_{1/6})MnO_3$, $(La_{0.8}Sr_{0.2})(Mn_{0.2}Fe_{0.2}Co_{0.4}Al_{0.2})O_3$ | Dual-scale porosity | 0.06 | ✓ | ✓ | ✓ | ✓ | ✓ | |

In the column of nominal power, the values reported with the symbol "∗" indicate the maximum incident radiative power reported in the study, since the nominal power of the reactor is not mentioned. In the column of morphology, the term "porous" indicates a reticulated porous structure with single-scale porosity. Notice that, although some of the works share commonalities in terms of modeling implementation, they are still reported here for the sake of completeness.



10.3389/fenrg.2025.1671615

materials. A more detailed discussion over the various morphologies proposed in literature is provided in Section 3.1.2.

In terms of operating conditions, multiphysics models focusing on the impact of flow rates on the cycle during reduction (*i.e.*, sweep gas) (Villafán-Vidales et al., 2011; Zhang and Smith, 2021; Orsini et al., 2024; Rojas et al., 2025) or oxidation [*i.e.*, steam (Lidor et al., 2021; Orsini et al., 2024), $CO_2$ (Bala Chandran and Davidson, 2016)], inlet fluid temperature (Pan et al., 2018), or incident radiation (Shu et al., 2021; Wang et al., 2025; Darfilal, 2020) were developed. Guene Lougou et al. (2018a) investigated the effect of different flow rates on the radiation losses from the system, indicating a significant increase at higher mass flow rates that counterbalance the enhanced convective heat transfer associated to the higher velocities in these conditions. Dai and Haussener (2022) provided an analysis of the optimal relation between the incident radiation and the optimal mass flow rate, including also a study over the optimal duration of the two steps. Considering the same reactor design, Wang et al. (2022) proposed a 2D dual-scale transport model. In this case, the incident radiation and the heat transfer process in the porous medium are considered on a macroscopic scale in the axial direction (fluid flow direction) and coupled with the diffusion process of oxygen vacancies in the radial direction considered on a microscopic scale. Zhang et al. (2018) performed a comparison of the results in terms of temperature and fluid flow distribution with respect to different thermal and transport models applied. A scale-up analysis of a directly irradiated reactor was proposed by Brendelberger et al. (2020) and Kyrimis et al. (2019), where different designs and operating conditions were analyzed in a MW-scale power plant. Similarly, Lampe et al. (2025b) considered the effect of a non-uniform irradiation on the hydrogen generation of a 250 kW plant. The results indicated a significant drop in terms of production rates and efficiency because of both local hot spots and non-uniform heating, up to 37% decrease in this second scenario.

#### 3.1.1.2 Indirectly irradiated reactors

As mentioned, the other big class of reactors are the indirectly irradiated systems. A specific type of indirectly irradiated configuration is represented by tubular reactors (Figure 5c), in which multiple tubes are placed in the cavity and filled with reactive material. The main advantage of this concept is the possibility to achieve continuous fuel production by alternatively performing the two steps in each element, having half of the tubes reducing and the other half oxidizing at all times. Martinek et al. (2014) carried out a performance evaluation of such a configuration for different geometrical designs, addressing the effect of different parameters including number, position, diameter of the tubes, and aperture of the window. Li et al. (2016) proposed a heat transfer model for a tubular reactor filled with a packed bed of ceria particles, by coupling a Monte Carlo ray tracing code for the radiation with a thermal lattice Boltzmann method for convection and diffusion, considering a constant oxygen partial pressure of 13 Pa. In the 3D heat and mass transfer models provided by Bader et al. (2015) (stress distributions assessment) and Bala Chandran and Davidson (2016) (impact of flow rates on production rates and temperature swing), each element is composed of two concentric alumina tubes with a packed bed of ceria particles in the internal annular region. The gas enters from the inner tube, and it is preheated by the exiting gases that flow in the outer tube, ensuring gas phase heat recovery. An alternative tubular reactor concept is provided by Yuan et al. (2016), where the solar-to-thermal conversion is separated from the thermal-to-chemical conversion in two different components coupled through a heat transfer fluid in the form of a liquid metal, with the aim of supplying efficiently the reaction heat to the oxygen storage material and perform sensible heat recuperation. Examples of tubular reactors containing moving redox particles have also been proposed. Li et al. (2020) considered a downward flow of ceria particles reacting with an upward flow of gas, analyzing the impact of different reaction kinetics conditions. The effect of particle size on the chemical reduction in a similar reactor is described by Valades-Pelayo et al. (2017). Falter and Pitz-Paal (2018) developed an example with counterflowing reducing and oxidizing particles to achieve sensible heat recuperation, focusing on the heat recovery effectiveness of this solution under different operating conditions.

A particular example of indirectly irradiated reactor is provided by Scott et al. (2024), in which the design was developed specifically to work in a RTS. The heat transfer model considers the reaction happening at the equilibrium in an environment with a fixed $O_2$ partial pressure of 10 Pa, and it was applied to evaluate the effect of various design choices on the performance of the redox cycle. Another cavity-type, indirectly irradiated reactor was proposed by Lanchi et al. (2013), proving the possibility to couple this configuration with the manganese-ferrite or similar cycles operating at moderate temperatures (750 °C–800 °C). The same thermochemical cycle and the same reactor were also proposed by Wang et al. (2021), where also the redox reaction was integrated in the model. Huang and Lin (2021) proposed a study on a cavity reactor with a 3D steady-state model, evaluating the differences in performance for directly and indirectly irradiated designs. From this comparative analysis, it resulted that the second option would limit the optical losses of the system, leading to an increased solar-to-fuel efficiency.

#### 3.1.1.3 Other reactors

Other models were developed based on different geometries or reactor types with the aim of integrating heat recovery techniques in the thermochemical cycle. A transient 3D model of a counter-rotating cylinders reactor (Figure 5e) with solid-solid heat recovery was proposed in 2014 by Lapp and Lipiński (2014) to benchmark the impact of different design and operational parameters on the global heat recovery effectiveness.

In recent years, one innovative solution was represented by moving redox units. The main advantage of this alternative approach resides in the possibility to continuously produce fuel incorporating heat recovery and counter current operation, resulting in increased theoretical performance limits. In this context, a few alternatives have been proposed. The R2Mx concept (Figure 5g), modelled by Vega Puga et al. (2024), consists of one separate reactor for each step with movable redox units, ensuring the potential benefits coming from spatially separating the two phases–namely, continuous fuel production and solid-phase heat recovery–while limiting the technical challenges associated with particle-based or rotating concepts. A scale-up analysis of the same type of reactor to a MW-scale was carried out by Brendelberger (2024), who compared the results of the heat transfer model with a state-of-the-art directly irradiated reactor. The results indicated important benefits for the proposed configuration in terms of temperature

distribution and maximum values reached in the redox material. Another approach is also represented by the concept of moving reactors proposed by Patankar et al. (2022). The RTS configuration would consist of multiple reactors cycling between a reduction and an oxidation zone, with the benefit of recovering solid-phase heat from the reactors exiting the reduction phase at a high temperature.

Under the modeling point of view, the abovementioned concepts require an appropriate implementation of the moving design, besides the intrinsic physics. We shall notice that, in relatively complex designs such as the RTS, modeling multiple reactors altogether would lead to notably increased computational cost and time. This implies that suitable techniques to simulate the entire reactor loop are needed, *e.g.*, by simplifying the numerical treatment with realistic assumptions (Patankar et al., 2022), reasonably customized on the specific design. In the R2Mx example (Vega Puga et al., 2024), the movement of the redox material was simulated by a sequential stepwise thermal approach, discretizing its trajectory into a few intermediate positions; at each step, the prior temperature field was imported as the initial condition and a transient heat transfer analysis (radiation, conduction, ambient losses) was run, with only two positions ultimately used since additional discretization changed the ceria enthalpy by only 0.22%.

An additional alternative developed in recent years is represented by reactors with redox materials in the form of membranes, guaranteeing continuous fuel production and gas-phase heat recovery. Wei et al. (2024) proposed a dense ceria tubular membrane reactor obtaining promising results in terms of performance despite the low conversion rate of $CO_2$ to CO with respect to theoretical predictions, suggesting the need to improve the membrane performance. Different conversion-limiting factors of the ceria membrane and their dependence on the operating conditions were analyzed by Pan et al. (2020), indicating the temperature as the main parameter to positively affect the conversion ratio of $CO_2$ to CO.

Besides the integration of heat recovery techniques, the oxygen removal from the reactive material during the endothermic reduction step is also crucial. State-of-the-art approaches integrate vacuum pumping or inert gas sweeping, but alternative concepts have been proposed with the aim of enhancing the reduction performance. A cascading pressure reactor (Figure 5d) was proposed by Singh et al. (2017), where a 1D transient model is transformed in a 2D and 3D steady-state solution through coordinate transformation and solutions combination. With this approach, the thermal reduction of redox particles is performed through multiple stages at decreasing pressures, resulting in a reduced pumping power demand with respect to the single-stage solution. The oxygen removal through the implementation of an electrolyte (*i.e.*, electrochemical oxygen removal) was modelled by Huang and Lin (2022), where the impact of this solution on the overall solar-to-fuel efficiency is compared with respect to the two traditional techniques (sweep gas injection and vacuum pumping) under different irradiance conditions. The concept of thermochemical oxygen pumping is described by Brendelberger et al. (2019b), where a second redox material is integrated (*i.e.*, an oxygen pumping material) to absorb the oxygen released by the first one (*i.e.*, the splitting material). The study indicated significant benefits in terms of pumping power reduction for pressures levels below 100 Pa.

### 3.1.2 Redox material

#### 3.1.2.1 Ceria

**3.1.2.1.1 Reticulated porous structures.** In most of the studies, the redox material considered is ceria in the form of reticulated porous foam, and it is modelled considering a uniform porosity across the whole reactive volume. Table 2 summarizes the main morphological parameters of the porous ceria structures adopted in literature. In this document, the term $\varepsilon$ indicates mm-scale porosity, while other structures (*e.g.*, dual-scale porosity) are indicated with specific subscripts. When the redox mass loading was not provided in the reference, it was estimated according to Equation 3 by using the total porous volume, $V_s$, and the effective density of the structure, $\rho_{s,eff}$.

$$m_{load} = (1-\varepsilon)\rho_{s,eff} V_s \tag{3}$$

Dai and Haussener (2022) evaluated the performance of a porous ceria monolith with a non-uniform porosity along the axial direction (that corresponds both to the fluid and irradiation directions). Specifically, linear, parabolic, and exponential distributions were evaluated in the model, keeping in all the cases an average porosity in the domain equal to 0.75. Mean pore diameter and specific surface area are extrapolated as functions of porosity according to Equations 4, 5, respectively (Suter et al., 2014):

$$d_{pore}(x) = 2.20 \cdot 10^{-3} \cdot \varepsilon(x) + 7.59 \cdot 10^{-4} \tag{4}$$

$$A_{sf}(x) = -2277.8 \cdot \varepsilon^2(x) + 2533.6 \cdot \varepsilon(x) + 262.3 \tag{5}$$

Dual-scale porosity RPC structures were also developed and manufactured. The dual-scale porosity RPC monolithic foams feature mm-scale pores ($\varepsilon_{mm}$) to enhance the volumetric absorption of solar radiation during reduction, and μm-scale pores ($\varepsilon_{\mu m}$) to increase the specific surface area and improve the mass transfer and the fuel production rates during oxidation (Lidor and Bulfin, 2024). Examples in which this morphology was implemented in a reactor model are collected in Table 3. In the study of Ackermann et al. (2017), a structure with different levels of porosity along the irradiation direction was tested. This example is characterized by a larger porosity on the irradiated side ($d_{pore,mm}$ equal to 2.2 mm) and a smaller one on the back side ($d_{pore,mm}$ equal to 0.6 mm). The results of this model were experimentally validated with two samples featuring 10 and 35 pores per inch (ppi) for the mm-scale ($\varepsilon_{mm}$ equal to 0.825 and 0.867, respectively). The μm-size porosity was 0.26 (mean pore diameter of 10 μm) for both samples.

**3.1.2.1.2 Reactive particles.** An alternative approach is represented by integrating the redox material as particles in the form of fixed beds, moving beds, or suspended in a fluidized bed. A summary of models based on this configuration, along with their specific parameters, is provided in Table 4.

#### 3.1.2.2 Alternative redox materials

Models that integrate alternative materials other than ceria are limited. Ma et al. (2024) investigated the performance of a porous monolith composed of $CeO_2$ and $ZrO_2$, with a mass ratio

TABLE 2 Morphological parameters of reticulated porous ceria components with mm-scale porosity implemented in the literature. The thickness represents the length of the porous medium in the irradiation direction.

| Ref. | $\varepsilon$ [-] | $d_{pore}$ [mm] | $n_{ppi}$ [-] | Thickness [mm] | $m_{load}$ [kg] |
|---|---|---|---|---|---|
| Lapp and Lipiński (2014) | 0.75 | 0.01 | — | 8 | 2.35* |
| Keene et al. (2014) | 0.6–0.9 | 0.01–1 | — | 20 | — |
| Lidor et al. (2021) | 0.7 | 2.3 | — | 30–45–60 | 53.3–213.1 |
| Wang et al. (2022) | 0.8 | 2 | — | 50 | — |
| Rojas et al. (2025) | — | — | — | — | — |
| Furler and Steinfeld (2015) | 0.63 | — | — | 100 | 1.413 |
| Orsini et al. (2024) | 0.7 | 2.3 | — | 60 | 0.22* |
| Brendelberger et al. (2020) | 0.762 | — | 10 | 25–55 | 127–466 |
| Lampe et al. (2025b) | 0.65 | 2.27 | 10 | 60 | 217 |
| Wang et al. (2025) | 0.9 | — | — | 24 | 0.29* |
| Cai et al. (2024) | 0.9 | — | — | 24 | 0.29* |
| Huang and Lin (2022) | 0.7 | $0.6{\cdot}10^{-3}$ | 35 | 6 | 0.07* |
| Dai and Haussener (2022) | $\varepsilon = f(x)$<br>$\varepsilon_{avg} = 0.75$ | Equation 4 | — | 10 | — |

The symbol "∗" indicates that the mass loading is not provided in the paper, and it was estimated according to Equation 3.

TABLE 3 Morphological parameters of dual-scale porous samples proposed in the literature. The thickness represents the length of the porous medium in the irradiation direction.

| Ref. | $\varepsilon_{mm}$ [-] | $\varepsilon_{\mu m}$ [-] | $\varepsilon_{dual}$ [-] | $d_{pore,mm}$ [mm] | $n_{ppi}$ [-] | Thickness [mm] | $m_{load}$ [kg] |
|---|---|---|---|---|---|---|---|
| Ackermann et al. (2017) | 0.825–0.867 | 0.26 | 0.87–0.9 | 0.6–2.2 | 10–35 | 25 | 0.046–0.035* |
| Zoller et al. (2019) | 0.6583 | 0.3561 | 0.78 | 2–7 | 3–10 | 25 | 18.38 |
| Scott et al. (2024) | — | — | 0.756 | — | — | 35 | 5.22 |
| Vega Puga et al. (2024) | — | — | 0.7622 | — | 10 | — | 1 |
| Brendelberger (2024) | 0.6583 | — | 0.78 | 2.015 | — | 35 | 20 |
| Kyrimis et al. (2019) | — | — | — | — | — | 25 | 145–1,478 |
| Zhao et al. (2025a) | 0.75 | 0.3 | 0.825 | 0.6 | 35 | 70 | 0.11* |

The symbol "∗" indicates that the mass loading is not provided in the paper, and it was estimated according to Equation 3, where $\varepsilon = \varepsilon_{dual}$.

of 1:1 between the two. Iron-manganese oxides were considered as packed beds by Wang et al. (2021) in the form of $(Mn_{0.33}Fe_{0.67})_2O_3$ within a 3D transient CFD model, and by Lanchi et al. (2013) in the form of $MnFe_2O_4$ within a 2D heat and mass transfer model, while Martinek et al. (2014) developed a study on a single-scale porosity RPC structure made of $Al_2O_3$ coated with reactive $CoFe_2O_4$ (hercynite material). Several examples considering ceramic foams (SiC and $Al_2O_3$) coated with $NiFe_2O_4$ were also proposed as single-scale porous structures (Villafán-Vidales et al., 2011; Guene Lougou et al., 2018a; Guene Lougou et al., 2018b; Shu et al., 2021), honeycomb structures (Lange et al., 2015) (Figure 5f), or packed beds (Darfilal, 2020). A SiC-based foam coated with $CuFe_2O_4$ and $Co_3O_4$ was modelled by Guene Lougou et al. (2023), indicating that this solution could provide a strong full solar spectrum absorption, but its application for $CO_2$ splitting does not represent a valid alternative due to SiC lower chemical stability at high temperature. Concerning the perovskite class of materials, Zhao et al. (2025a) recently provided a performance comparison of state-of-the-art ceria ($CeO_2$), Zr-doped ceria ($Zr_{0.15}Ce_{0.85}O_2$ (Zr15)), and two perovskites ($La_{0.6}Ca_{0.4}Mn_{0.6}Al_{0.4}O_3$ (LCMA) and $La_{0.8}Sr_{0.2}MnO_3$ (LSM82)), by proposing a multi-scale modeling framework composed of a system-level model, including heat

TABLE 4 Morphological parameters of particle-based reactors proposed in the literature.

| Ref. | Particles bed type | N° of tubes | $d_p$ [mm] | $\varepsilon$ [-] | $m_{load}$ |
|---|---|---|---|---|---|
| Bala Chandran and Davidson (2016) | Packed bed | 6 | 5 | 0.45 | 0.59 [kg/tube] |
| Li et al. (2016) | Packed bed | 14 | — | 0.776 | 0.70 [kg/tube] |
| Bader et al. (2015) | Packed bed | 7 | 4 | 0.45 | 0.71 [kg/tube] |
| Zhang and Smith (2021) | Packed bed | — | 3–6 | 0.33 | — |
| Zhang and Smith (2019) | Packed bed | — | 5 | 0.65 | — |
| Yuan et al. (2016) | Packed bed | 8 | 0.01 | 0.6 | — |
| Sedighi et al. (2021) | Packed bed | — | 19–43 | 0.48 | — |
| Falter and Pitz-Paal (2018) | Moving bed | 2 | 0.004–0.01 | — | 10 [g/s] |
| Li et al. (2020) | Moving bed | 1 | 0.05–0.1 | — | 0.025–0.15 [g/s] |
| Singh et al. (2017) | Moving bed | — | 0.25 | — | 2 [g/s] |
| Bellan et al. (2019) | Fluidized bed | — | 1 | — | — |
| Valades-Pelayo et al. (2017) | Fluidized bed | 9 | 0.001–0.02 | — | — |
| Bellan et al. (2018b) | Fluidized bed | — | 7–14 | — | — |

exchangers and gas separation, and a detailed multiphysical model describing a generic packed bed reactor, incorporating fluid flow, heat transfer, mass transfer, and thermochemical reactions. The results displayed higher hydrogen production and solar-to-fuel efficiency when ceria was implemented, while the alternatives were mainly limited by slower oxidation kinetics associated to smaller reaction enthalpy. On the other hand, thanks to this thermodynamic feature, the implementation of perovskites enabled lower reduction temperatures. In a follow-up work (Zhao et al., 2025b), the same authors used the previously developed model to compare ceria with another series of perovskites ($La_{0.6}Ca_{0.4}Mn_{0.6}Al_{0.4}O_3$ (LCMA), $CaTi_{0.5}Mn_{0.5}O_3$ (CTM55), $(La_{1/6}Pr_{1/6}Nd_{1/6}Gd_{1/6}Sr_{1/6}Ba_{1/6})MnO_3$ (LPNGSBMn), and $(La_{0.8}Sr_{0.2})$ $(Mn_{0.2}Fe_{0.2}Co_{0.4}Al_{0.2})O_3$ ($LSMFC_{0.4}A$)), with ceria exhibiting superior performance overall. In general, the present research highlighted that perovskite-based reactor models implementing detailed and high-fidelity physics are numerically limited in the literature up to date. Possible reasons explaining this gap could be, among others: (i) lack of well-established and/or widely used thermophysical properties (*e.g.*, heat capacity, thermal conductivity), as well as optical and radiative properties [*e.g.*, surface reflectance and emittance (Ackermann et al., 2017)] for alternative redox materials, especially for novel perovskite compositions that were synthesized and tested only at the laboratory scale in relatively small amounts; (ii) relatively limited experimental demonstrations of reactor-size actual reactive porous structures made of perovskites (Haeussler et al., 2020c; Gager et al., 2022; Pérez et al., 2024); (iii) uncertainty in the achievable efficiency when novel perovskites would be tested on-field under realistic operating conditions, as opposed to idealized laboratory conditions (Lou et al., 2024). Thermodynamic models are common in the literature to estimate the upper boundaries in the process efficiency (Lidor and Bulfin, 2024), and such models have also been reported for perovskites (Lou et al., 2024; Lou et al., 2022). However, these models are generally zero-dimensional (0D), assuming that the redox material volume is sufficiently small for temperature and concentration gradients to be neglected, while also relying on thermodynamic equilibrium chemistry. These considerations strongly emphasize the need to develop higher-dimensional continuum-level reactor models using perovskites as the active redox material. Spatial effects–such as heat and mass transport limitations, temperature gradients across the porous volume, and accumulation of reaction products –, as well as finite-rate chemistry (*i.e.*, kinetics), can play a crucial role in accurately predicting the actual performance, especially under realistic operating conditions compared to idealized laboratory testing. Finally, some works did not consider any redox material in the model and focused on the other physics without including chemistry. In these cases, a chemically inert material is considered and only its effect on heat transfer and fluid flow is analyzed, neglecting the chemical interactions with the fluid phase. Huang and Lin (2021) and Zhang et al. (2018) developed studies considering a SiC-based porous monolith, while in the work by Pan et al. (2018) the composition of the sample is not specified. Similarly, a reactor containing a fluidized bed of inert particles is proposed by Bellan et al. (2019) and Sedighi et al. (2021).

## 3.2 Modeling approaches and assumptions

Regardless of the accuracy and level of detail of each specific model, the studies available in the literature describe the main physical processes starting from the same principles of mass,

momentum, and energy conservation. The main differences between the different modeling approaches mostly lie in the description of the chemistry of the reaction and of the radiative heat transfer. In this section, a panoramic overview of the main approaches implemented throughout the literature to model the different physical phenomena is provided.

### 3.2.1 Mass and momentum transfer modeling

The mass transfer in solar thermochemical reactors is characterized by a fluid phase and a solid phase, with the gaseous species that could either be generated or consumed by chemical reactions. The conservation of the $i^{th}$ species in the gas mixture is governed by Equation 6, where $w_i$ is its specific mass fraction.

$$\frac{\partial}{\partial t}\left(\varepsilon\rho_{\mathrm{f}}w_i\right)+\nabla\cdot\left(\varepsilon\rho_{\mathrm{f}}\mathbf{u}w_i\right)=\nabla\cdot\left(\rho_{\mathrm{f}}D_i\nabla w_i\right)+r_i \tag{6}$$

The main mass transfer mechanisms are advection, accounted for through the term $\nabla\cdot\left(\rho_{\mathrm{f}}\mathbf{u}w_i\right)$ and obtained from the momentum equation, and diffusion, modelled by the term $\nabla\cdot\left(\rho_{\mathrm{f}}D_i\nabla w_i\right)$. $D_i$ represents the Brownian diffusion coefficient (Guene Lougou et al., 2023; Valades-Pelayo et al., 2017). In addition, the contribution of the chemical reaction is considered by the source/sink term $r_i$, whose accurate modeling is of central importance. The expression used for this term strongly depends on how the reduction and oxidation processes of the redox material are modelled. A more specific discussion on the several approaches proposed is provided in Section 3.2.3.

The mass and momentum conservation inside the porous medium are expressed according to Equation 7 and Equation 8 as incompressible Navier-Stokes equations. $\boldsymbol{\tau}$ is the stress tensor evaluated according to Equation 9, where $\hat{\mathbf{I}}$ indicates the identity matrix and $\mu$ the dynamic viscosity of the fluid. With the assumption of dilute mass transfer, the contribution of the chemical reaction to the mass conservation is neglected by excluding the right term of Equation 7, leading to a deviation in the velocity field that is reflected in the temperature and concentration distributions (Wang et al., 2022; Sharma et al., 2023; Rojas et al., 2025; Wang et al., 2025).

$$\nabla\cdot\left(\varepsilon\rho_{\mathrm{f}}\mathbf{u}\right)=\sum_i r_i \tag{7}$$

$$\frac{\partial}{\partial t}\left(\varepsilon\rho_{f}\mathbf{u}\right)+\nabla\cdot\left(\varepsilon\rho_{\mathrm{f}}\mathbf{u}\mathbf{u}\right)=-\nabla p+\nabla\cdot\boldsymbol{\tau}+\mathbf{S}_{\mathrm{porous}} \tag{8}$$

$$\boldsymbol{\tau}=\mu\left(\nabla\mathbf{u}+\nabla\mathbf{u}^{\mathrm{T}}\right)-\frac{2}{3}\mu(\nabla\cdot\mathbf{u})\hat{\mathbf{I}} \tag{9}$$

In general, low Reynolds numbers are considered inside the reactor, and the fluid flow regime is typically assumed to be laminar. A turbulent flow has been considered by Ophoff et al. (2020), who applied the realizable $k-\varepsilon$ model in which two additional equations for the turbulence kinetic energy, $k$, and the turbulence kinetic energy dissipation rate, $\varepsilon$, are solved. The work focuses only on the temperature field inside the reactor without implementing any reactive material. A comparison between three different turbulence models (standard $k-\varepsilon$, RNG $k-\varepsilon$, and SST $k-\omega$) is provided by Sedighi et al. (2021), indicating that the pressure drop in the packed bed is accurately described by all the models, while only the second and third ones are accurate for the heat transfer. Also in this case, no chemistry was implemented.

Overall, turbulence modeling for solar thermochemical fuel production remains limited, although the impact of a turbulent flow on the overall performance could be significant in terms of heat transfer, as well as of chemical species transport, with consequent improvement in the reaction rates (Wheeler et al., 2017). Moreover, perovskites are difficult to reoxidize, and their higher fuel yields come with a significant water-heating penalty (Li et al., 2022). This means that the optimal operating point for a perovskite-based reactor could involve larger oxidant flow rates during the oxidation step. For context, Lou et al. (2024) estimated that some perovskites exhibit their optimal performance at a steam flow rate one order of magnitude larger than ceria, under specific conditions. Thus, in principle, the fluid flow analysis could benefit from including turbulence as a possible operating regime–importantly, depending on the specific reactor design, geometry, and flow field configuration–in order to explore a wider operational window, as well as to get accurate results under the selected conditions. At the same time, operating in a turbulent regime could generate higher energy penalties in terms of sweep gas and/or oxidant requirements (Davenport et al., 2016), and hence, the implementation of clever heat recovery strategies could become even more relevant to ensure competitive performance. Overall, given that a real demonstration of perovskite-based reactors operation is not well represented up to date, there is wide room for numerical investigation in terms of optimal operating conditions for this class of systems.

The momentum source term, $\mathbf{S}_{\mathrm{porous}}$, represents the additional pressure drops induced on the flow by the presence of the porous medium. This term is generally evaluated by using well established relations such as the Darcy's law (Huang and Lin, 2021; Lanchi et al., 2013; Keene et al., 2014; Kyrimis et al., 2019; Cai et al., 2024; Wang et al., 2025; Martinek et al., 2014) (Equation 10) and the extended Darcy–Forchheimer expression (Bader et al., 2015; Furler and Steinfeld, 2015; Ackermann et al., 2017; Guene Lougou et al., 2018b; Pan et al., 2018; Huang and Lin, 2022; Dai and Haussener, 2022; Sharma et al., 2023; Guene Lougou et al., 2023; Ma et al., 2024; Orsini et al., 2024; Lampe et al., 2025a; Lampe et al., 2025b; Bala Chandran and Davidson, 2016) (Equation 11), necessary for Reynolds numbers higher than 1 (Wheeler et al., 2017).

$$\mathbf{S}_{\mathrm{porous}}=-\frac{\mu_{\mathrm{f}}}{K}\mathbf{u} \tag{10}$$

$$\mathbf{S}_{\mathrm{porous}}=-\frac{\mu_{\mathrm{f}}}{K}\mathbf{u}-\rho_{\mathrm{f}}F_{\mathrm{D}}|\mathbf{u}|\mathbf{u} \tag{11}$$

In these equations, $K$ represents the effective permeability of the redox material, while $F_{\mathrm{D}}$ is the Dupuit–Forchheimer coefficient. Other approaches evaluate this term through a flow resistance coefficient according to the Ergun equation (Wang et al., 2022), or by considering particle/fluid interactions through a discrete element method (Zhang and Smith, 2021). In addition, Wu et al. (2010) proposed a model for the pressure drop estimation in a packed bed based on experimental and numerical results. The relations depend on porosity and mean cell size of the reactive media and under its range of applicability ($\varepsilon$ in the range 0.66–0.93, $Re$ in the range 10–400) was proved to provide a better estimation with respect to the Darcy–Forchheimer law (Zhang et al., 2018). Regarding the membrane reactor proposed by Pan et al. (2020), the momentum source term associated to the reaction surface was assumed negligible.

In case the redox material is constituted by elements that are not fixed in space (such as fluidized bed or moving particles), its motion is modelled according to different methods depending on the volume occupied by the solid particles (Grobbel et al., 2019). In case of dilute fluidized regime, the particle-particle interactions are negligible and the Lagrangian approach is usually applied (Li et al., 2020). Another approach is provided by Valades-Pelayo et al. (2017), where the particle motion inside the tubes is assumed to be a fully developed laminar flow with parabolic shape with respect to the radial direction. On the other hand, for dense fluidized regimes (moving beds) the particle motion is usually modelled through the Lagrangian-Eulerian approach solved with the discrete element method (DEM) (Zhang and Smith, 2019; Zhang and Smith, 2021; Bellan et al., 2022). For each particle, the force balance is solved including the particle interactions as indicated in Equations 12, 13 (translational and rotational motion, respectively). In this formulation, $\mathbf{F}_{\text{aero}}$ represents aerodynamic forces (drag, pressure gradient), $\mathbf{F}_{\text{g}}$ the volume forces (buoyancy and gravity) and $\mathbf{F}^{\text{n}}_{\text{con}}$, $\mathbf{F}^{\text{t}}_{\text{con}}$ the normal and tangential contact forces due to interactions (particle-particle, particle-wall).

$$m_{\text{p}}\frac{\text{d}\mathbf{u}_{\text{p}}}{\text{d}t} = \mathbf{F}_{\text{aero}} + \mathbf{F}_{\text{g}} + \mathbf{F}^{\text{n}}_{\text{con}} + \mathbf{F}^{\text{t}}_{\text{con}} \tag{12}$$

$$\mathbf{I}_{\text{p}}\frac{\text{d}\boldsymbol{\omega}_{\text{p}}}{\text{d}t} = \boldsymbol{\tau}_{\text{p}} \tag{13}$$

### 3.2.2 Heat transfer modeling, and thermomechanical analysis

To solve the energy balance inside the reactor, two main approaches are typically followed. In the first case, local thermal equilibrium (LTE) is assumed, meaning that the solid and gaseous phases of the porous medium are assumed to be at the same temperature in each point of the porous domain, and thus a single energy equation is solved. This assumption is considered valid if the expected temperature difference between the two phases is lower than the characteristic temperature differences in the whole reactor (Wheeler et al., 2017). The energy conservation expressed by Equation 14 is solved for both the fluid and the solid phases together (Lanchi et al., 2013; Guene Lougou et al., 2018b; Zhang and Smith, 2019; Martinek et al., 2014; Yuan et al., 2016; Vega Puga et al., 2024).

$$\begin{aligned}\frac{\partial}{\partial t}\left(\varepsilon\rho_{\text{f}}\sum_i Y_i h_{i,\text{f}} + (1-\varepsilon)\rho_{\text{s}}h_{\text{s}}\right) + \nabla\cdot\left(\rho_{\text{f}}\mathbf{u}\sum_i Y_i h_{i,\text{f}}\right)\\ = \nabla\cdot\left(\left(k_{\text{s,eff}} + k_{\text{f,eff}}\right)\nabla T\right) - \nabla\cdot\mathbf{q}_{\text{rad}} + Q_{\text{reaction}}\end{aligned} \tag{14}$$

On the other hand, with the local thermal non-equilibrium (LTNE) approach, the two phases are assumed to be at different temperatures, and one equation for each phase needs to be solved (Equation 15 for the fluid; Equation 16 for the solid) (Brendelberger et al., 2020; Lange et al., 2015; Bellan et al., 2019; Villafán-Vidales et al., 2011; Kyrimis et al., 2019; Sharma et al., 2023; Guene Lougou et al., 2023; Cai et al., 2024; Orsini et al., 2024; Lampe et al., 2025b; Zhao et al., 2025a; Darfilal, 2020). The two energy equations are then coupled through the convection term $Q_{\text{sf}}$ (Equation 17), expressing the interfacial heat transfer between the two phases in the pores. This approach is in general more suitable for reactors with a high redox mass loading, such as stationary systems with porous samples or packed beds of particles (Wheeler et al., 2017). In the example developed by Huang and Lin (2022), the energy conservation is solved depending on the oxygen removal strategy, that is directly related to the Reynolds number: specifically, LTNE is applied in the case of inert sweep gas, while for vacuum and electrochemical pumping LTE is assumed to be sufficient due to the negligible flow associated with these options [$Re < 0.23$ (Kim and Jang, 2002)]. A comparison of the temperature fields of a solar reactor obtained with these two approaches is provided by Zhang et al. (2018), indicating that the average temperature deviation between the solid and fluid phases increases by ten times for a velocity increase from 0.005 to 0.5 m/s.

$$\frac{\partial}{\partial t}\left(\varepsilon\rho_{\text{f}}\sum_i Y_i h_{i,\text{f}}\right) + \nabla\cdot\left(\rho_{\text{f}}\mathbf{u}\sum_i Y_i h_{i,\text{f}}\right) = \nabla\cdot\left(\varepsilon k_{\text{f}}(\nabla T)\right) + Q_{\text{sf}} \tag{15}$$

$$\frac{\partial}{\partial t}\left((1-\varepsilon)\rho_{\text{s}}h_{\text{s}}\right) = \nabla\cdot\left(k_{\text{s,eff}}(\nabla T)\right) - \nabla\cdot\mathbf{q}_{\text{rad}} + Q_{\text{reaction}} - Q_{\text{s,f}} \tag{16}$$

$$Q_{\text{sf}} = h_{\text{sf}}A_{\text{sf}}\left(T_{\text{s}} - T_{\text{f}}\right) \tag{17}$$

$$Q_{\text{reaction}} = \frac{r_{\text{O}_2}(\delta)\cdot\Delta h_{\text{red}}(\delta)}{MM_{\text{O}_2}} \tag{18}$$

The term $Q_{\text{reaction}}$ (Equation 18) accounts for the reaction heat and it is assumed to be developed in the solid phase and transferred to the fluid by interfacial convection (Orsini et al., 2024). The term $\nabla\cdot\mathbf{q}_{\text{rad}}$ represents the radiative heat source absorbed by the reactive material and does not appear in the fluid equation, since the fluid phase is generally considered as a transparent medium in the radiative heat transfer modeling (Keene et al., 2014; Pan et al., 2018; Ma et al., 2024; Lampe et al., 2025b). This latter contribution represents another critical element in the modeling step, since a formal homogenization method for the radiative heat equation is not available yet in literature (Wheeler et al., 2017). A more detailed discussion of the approaches applied in the main studies on this specific topic is reported in Section 3.2.4.

Simulating alternative materials other than ceria, including widely explored perovskites, also implies the need to accurately know, among others, their thermophysical properties appearing in the above equations, such as thermal conductivity and heat capacity. In principle, these properties could significantly span over a relatively wide range, and by common sense, some degree of uncertainty needs to be considered especially for novel synthesized compositions. For instance, Muhich et al. (2018) assumed 80 J/mol/K and 140 J/mol/K for the heat capacity of ceria and La-based perovskites, respectively, evidencing an important difference between the two values. We shall notice how variations in thermophysical properties can significantly affect heat transfer and the resulting temperature distribution within the porous redox structure, thereby directly influencing its spatially dependent reactivity and utilization. Moreover, a higher heat capacity also means that more heat will be needed to bring the redox mass up to a given reduction temperature, with direct implications on the energy balance around the reactor, and potentially on the performance metrics.

The heat transfer analysis represents a key starting point to additional critical reactor engineering considerations required

during the design stage, such as the evaluation of thermal stresses inside the reaction chamber. Due to the high temperature and pressure differences to withstand, an accurate analysis needs to be carried out to correctly size each component. In spite of this, a limited number of multiphysics models include also thermomechanical and thermal stress considerations and the knowledge of the impact of these factors on solar thermochemical reactors is still limited (Zhang et al., 2020).

Scott et al. (2024) proposed a simplified structural mechanics model with a finite element method in COMSOL Multiphysics® to determine the thickness of the window and flange, by neglecting possible tensile stress concentrations, thermal expansion, and creep effects. A more detailed analysis on a cavity-type reactor is provided by Zhang et al. (2020), where the maximum compressive stress and the Von Mises stresses have been evaluated according to the 3D temperature profiles through the specific software ANSYS Mechanical APDL® 16.0. The results highlighted the strong impact of thermal expansion, indicating that the reduction of highly concentrated compressive stresses associated with this phenomenon would strongly reduce ceramic breakage. A similar study has been performed by Huang et al. (2024), where the effects of incident solar power and inner walls emissivity on the thermal stresses have been described. Furthermore, the study indicated that the operating conditions of the fluid (working pressure and gas velocity) do not have a strong influence in this respect. Bader et al. (2015) implemented a thermomechanical analysis in the model for a tubular reactor in order to evaluate the stress distribution over the outer surface of each tube due to temperature gradients. The initial section of the tubes was estimated by applying a 1D analysis and assuming constant outer temperature and uniform heat flux, while a more accurate 3D linear elastic finite element model is reported based on the temperature profiles extrapolated from the heat and mass transfer physics. A thermal stress analysis elaborated for a tubular reactor designed for stoichiometric reduction of metal oxides is proposed by Wang et al. (2020), where an effective stress is evaluated according to the Von Mises theory.

### 3.2.3 Chemical reaction modeling

The modeling of the redox reaction is key in the multiphysics simulation of a thermochemical cycle since it couples the chemistry with mass and reactive species conservation. In particular, the aim is to evaluate the variation of reactants and products through the determination of the source/sink term $r_i$ in Equation 6. The possibility to accurately model the chemical reaction depends on the specific redox material implemented, as well as on the availability of studies on their thermochemical and kinetic properties (Wheeler et al., 2017). The reduction extent $\delta$ of the solid redox material is typically described as a function of temperature and oxygen partial pressure by applying experimental or analytical functions, with the source term of a generic species in the gas phase–expressed in $\mathrm{kg/(m^3 s)}$ – derived from Equation 19. The subscript $i$ represents the different gaseous species involved in the redox reaction, with $\nu_i$ being the corresponding stoichiometric coefficient (0.5 for $O_2$, −1 for $H_2O$ and $CO_2$, 1 for $H_2$ and CO). The subscript s indicates the solid redox material.

$$r_i = \rho_{s,\mathrm{eff}} \cdot \frac{\nu_i \cdot MM_i}{MM_s} \cdot \frac{\mathrm{d}\delta}{\mathrm{d}t} \tag{19}$$

#### 3.2.3.1 Ceria reduction modeling

The majority of the multiphysics models available in the literature implement ceria as the redox material. An important number of studies proposed with ceria consider the thermodynamic equilibrium between the solid and the gas phases. This assumption is well-motivated by the fast kinetics that leads to a good approximation of the real reaction, especially in the reduction step (Ackermann et al., 2017). A comparison between an equilibrium model describing the $CO_2$ splitting reaction for CO production and experimental measures on a fixed bed of ceria particles is provided by Venstrom et al. (2015). The study indicates that the equilibrium assumption fits the experimental data for a wide range of temperatures and flow rates in the reduction step, while in the oxidation step it is valid only up to a given $CO_2$ flow rate, and therefore, in this case the kinetics should be included for a better representation of the reaction mechanism. Besides the integration of the kinetics of reaction, another significant difference between the proposed models resides in the number of steps modelled. In fact, in many cases, the analysis was simplified by considering only the reduction step and the material was often considered to be completely re-oxidized from the resulting state at the end of the reduction step (Scott et al., 2024; Brendelberger, 2024; Ackermann et al., 2017; Kyrimis et al., 2019; Vega Puga et al., 2024).

An expression for ceria nonstoichiometry assuming thermodynamic equilibrium is proposed by Bulfin et al. (2013) based on the Arrhenius equation, with the free parameters $x$ (maximum reduction extent), $n$ (oxygen partial pressure exponent), $\Delta E = E_{red} - E_{ox}$ (difference between reduction and oxidation activation energies), and $\frac{A_{red}}{A_{ox}}$ (ratio between reduction and oxidation preexponential factors) derived from linear fits on experimental data (Equation 20) (Panlener et al., 1975; Zinkevich et al., 2006). This relation was implemented in several studies that considered only the reduction step (Brendelberger, 2024; Li et al., 2020; Zhang and Smith, 2019; Zhang and Smith, 2021; Sharma et al., 2023; Li et al., 2016; Brendelberger et al., 2019b).

$$\left(\frac{\delta}{x-\delta}\right) = \frac{A_{red}}{A_{ox}} \cdot p_{O_2}^{-n} \cdot e^{-\frac{\Delta E}{RT}} \tag{20}$$

The same authors proposed an updated expression in a following study. In this case, the analytical expression (Equation 21) was derived from thermodynamic considerations on the Gibbs free energy and the entropy of reduction, fitting the obtained curves with experimental measures conducted on porous granules of ceria (Bulfin et al., 2016). The main difference from the previous model is that the variation of the enthalpy of reaction against nonstoichiometry is also included. For completeness, Equations 22, 23 report the thermodynamic functions as typically expressed for the nonstoichiometric reduction reaction (Bulfin et al., 2017), in which the subscript $\delta$ indicates that they are defined as partial molar quantities, $\Delta g_\delta \equiv \frac{\partial \Delta g}{\partial \delta}$, and the circular superscript refers to the standard pressure (Bulfin et al., 2016). These thermochemical properties, namely, reduction enthalpy, $\Delta h^\circ_\delta(\delta)$, and entropy, $\Delta s^\circ_\delta(\delta)$, have been extracted for several nonstoichiometric oxides, notably ceria, ceria-zirconia, and several perovskites (Takacs et al., 2015; Panlener, 2025; Yang et al., 2014; Takacs et al., 2016; Hao et al., 2014; Ezbiri et al., 2017; Qian et al., 2020; Qian et al., 2021), and have a key role in determining the material behavior and eventually

the process performance. To achieve efficient operation in two-step thermochemical cycles, low $\Delta h^{\circ}_{\delta}(\delta)$ at larger reduction extents (*i.e.*, larger $\delta$) and high $\Delta s^{\circ}_{\delta}(\delta)$ should be addressed. The former allows for reducing the oxygen carrier at more moderate temperatures, while the latter permits smaller $\Delta T$ swing between the two cycle steps and allows for a stronger thermodynamic driving force (Carrillo and Scheffe, 2017). Moreover, a high $\Delta h^{\circ}_{\delta}(\delta)$ at lower nonstoichiometry allows the oxidation step to be performed at higher temperatures, thus reducing the temperature swing (Carrillo and Scheffe, 2017).

$$\left(\frac{\delta}{x-\delta}\right)^{n} = \left(\frac{p_{O_2}}{p_0}\right)^{-0.5} \cdot e^{\frac{\Delta s_{red}}{R}} \cdot e^{\frac{\Delta h_{red}(\delta)}{RT}} \tag{21}$$

$$\Delta g_{\delta} = \Delta g^{\circ}_{\delta} + \frac{1}{2} RT \ln\left(\frac{p_{O_2}}{p^{\circ}}\right) \tag{22}$$

$$\Delta g^{\circ}_{\delta} = \Delta h^{\circ}_{\delta} - T\Delta s^{\circ}_{\delta} \tag{23}$$

In the work developed by Ackermann et al. (Ackermann et al., 2017) only the reduction of ceria was as well simulated, assuming thermodynamic equilibrium and applying an oxygen defect model to fit experimental thermogravimetric measurements (Panlener et al., 1975). With this approach, the nonstoichiometry $\delta$ as a function of temperature and oxygen partial pressure is expressed according to Equation 24 (with T in °C). The same expression has been integrated by Zoller et al. (2019), Wang et al. (2025), and Kyrimis et al. (2019).

$$\delta = 10^{-(2.15\cdot10^{-6}\cdot T^2 - 9.88\cdot10^{-3}\cdot T + 12.21)} \cdot \left(\frac{p_{O_2}}{p_0}\right)^{1.25\cdot10^{-7}\cdot T^2 - 3.10\cdot10^{-4}\cdot T - 1.83\cdot10^{-2}} \tag{24}$$

A similar approach was followed by Furler and Steinfeld (2015), where the same experimental data from (Panlener et al., 1975) are fitted accordingly to the procedure described in other studies (Scheffe and Steinfeld, 2012; Erman et al., 2013). This procedure led to the relation for the equilibrium nonstoichiometry $\delta$ as function of temperature and oxygen partial pressure as expressed in Equation 25.

$$\begin{aligned}\log(\delta) = {} & a_1 + a_2 \cdot \log\left(\frac{p_{O_2}}{p_0}\right) + a_3 \cdot \log\left(\frac{p_{O_2}}{p_0}\right)^2 \\ & + a_4 \cdot \log\left(\frac{p_{O_2}}{p_0}\right)^3 + a_5 \cdot T + a_6 \cdot \log\left(\frac{p_{O_2}}{p_0}\right) \cdot T \\ & + a_7 \cdot \log\left(\frac{p_{O_2}}{p_0}\right)^2 \cdot T + a_8 \cdot \log\left(\frac{p_{O_2}}{p_0}\right) \cdot T^2\end{aligned} \tag{25}$$

Keene et al. (2014) proposed a solid-gas interface kinetics to model the reduction of ceria. By assuming singly ionized oxygen vacancies, the oxygen released is extrapolated to the law of mass action described in Equation 26. The study reported a lack of experimental data on the kinetics of reduction, and as a consequence, the rate constant $k_{red}$ was assumed sufficiently high to ensure the equilibrium, considering that the reaction would be limited mainly by the heating rate of the solid rather than by its kinetics.

$$r_{O_2} = \frac{MM_{O_2}}{2} k_{red} \left[ e^{\frac{\Delta h_{red} - T\Delta s_{red}}{2RT}} \delta^2 - \left(\frac{p_{O_2}}{p_0}\right)^{\frac{1}{2}} \delta^2 \right] \tag{26}$$

#### 3.2.3.2 Ceria reduction and oxidation modeling

In the studies proposed by Lapp and Lipiński (2014), Vega Puga et al. (2024), and Brendelberger et al. (2020), both reduction and oxidation were implemented in the model assuming the reaction being at the equilibrium in both the cycle steps, and neglecting the fluid flow. In the first case, the reduction zone was modelled with the same approach implemented in Scott et al. (2024) considering a constant oxygen partial pressure of 0.01 atm, while for the oxidation zone, the reaction was assumed to reach its completion at the temperatures considered in the study case, with the nonstoichiometry supposed to decrease linearly to zero across that region. In the second model, Equation 24 was applied to both steps, with the oxygen partial pressure during the oxidation derived from the expression of the equilibrium constant for the water splitting reaction (Equation 27) as a function of the water conversion factor, $X_{ox}$ (Equation 28). The same approach was also applied in the third case, where the oxidation was simulated with $CO_2$ instead of $H_2O$.

$$p_{O_2,ox} = p_0 \left( \frac{K_{eq}(1 - X_{ox})}{X_{ox}} \right)^2 \tag{27}$$

$$X_{ox} = \frac{n_{H_2}}{n_{H_2O}} = \frac{(\delta_{red} - \delta_{ox}) n_{CeO_2}}{n_{H_2O}} \tag{28}$$

A reaction rate that models both ceria reduction and re-oxidation kinetics in an oxygen-containing atmosphere was proposed by Bulfin et al. (2013), and was integrated by Rojas et al. (2025) and Ma et al. (2024). With this approach, the diffusion process is considered as the diffusion of oxygen vacancies and the diffusion coefficient is well described by the Arrhenius dependence on temperature. The reaction rate constant is then determined by the balance between reduction and oxidation terms, resulting in Equation 29. In this case, the free parameters were obtained from experimental measures performed in the same study on ceria pellets (Bulfin et al., 2013).

$$\frac{d\delta}{dt} = (x - \delta) A_{red} \cdot e^{-\frac{E_{red}}{RT}} - \delta p^{n}_{O_2} A_{ox} \cdot e^{-\frac{E_{ox}}{RT}} \tag{29}$$

This expression was extended in the work provided by Lampe et al. (2025b) to account for the actual amount of steam and sweep gas required to run the reactions. With this purpose, Equation 29 is multiplied to an equilibrium conversion ratio, defined according to Equation 30 for the oxidation step and equal to one for the reduction. $n_{H_2O,act}$ and $n_{H_2O,req}$ represent the available and required amount of steam to run the oxidation as a function of temperature, oxygen partial pressure, and fraction of the reaction completed, $\alpha$, respectively.

$$\gamma\left(T, T_{red}, p_{O_2}, \alpha\right) = min\left( \frac{n_{H_2O,act}}{n_{H_2O,req}\left(T, T_{red}, p_{O_2}, \alpha\right)}; 1 \right) \tag{30}$$

Bala Chandran and Davidson (2016) implemented the kinetics for both phases of the reaction in a $CO_2$ atmosphere applying a modified form of Equation 29 in order to reduce the number of dependent parameters. By imposing the equilibrium constraint that relates reduction and oxidation rate according to Equation 31, Equation 32 for the global rate of reaction is obtained (with $p_{O_2,eq}$ representing the oxygen partial pressure in equilibrium conditions). The oxidation rate is always expressed according to

the Arrhenius equation. In addition, direct thermal dissociation of $CO_2$ was considered since it was proved to be significant at high temperatures. It follows that the total oxygen release rate from direct dissociation and release/uptake from ceria can be expressed by combining the two contributions.

$$k_{red} = k_{ox} \cdot \left( \frac{p_{O_2,eq}}{p_0} \right)^n \tag{31}$$

$$\frac{d\delta}{dt} = k_{ox}\delta \left[ \left( \frac{p_{O_2,eq}}{p_0} \right)^n - \left( \frac{p_{O_2}}{p_0} \right)^n \right] \tag{32}$$

The same approach proposed by Keene et al. (2014) and described above was also adopted by Dai and Haussener (2022) and Zhao et al. (2025a), Zhao et al. (2025b), but in these cases, doubly-ionized vacancies were considered as the main mechanism for oxygen diffusion. Consequently, the expression for the oxygen release capacity was modified according to Equation 33. In contrast to the previous models, in this paper the oxidation step was also implemented in the model, expressing the hydrogen release rate according to Equation 34. The reduction rate constant, $k_{red}$, was considered equal to $10^{-3}\ \frac{mol}{m^2 s}$, while the oxidation rate constant was expressed as a function of temperature and reactive surface area (Equation 35). A similar method was proposed by Huang and Lin (2022) and Yuan et al. (2016).

$$r_{O_2} = \frac{MM_{O_2}}{2} A_{sf} \cdot k_{red} \left[ e^{\frac{\Delta h_{red} - T\Delta s_{red}}{2RT}} \delta^3 - \left( \frac{p_{O_2}}{p_0} \right)^{\frac{1}{2}} \delta^3 \right] \tag{33}$$

$$r_{H_2} = -MM_{H_2} A_{sf} \cdot k_{ox} \left[ e^{\frac{\Delta g_{H_2O} + \frac{1}{2}(-\Delta h_{red} + T\Delta s_{red})}{RT}} \left( \frac{p_{H_2}}{p_0} \right) \delta^3 - \left( \frac{p_{H_2O}}{p_0} \right) \delta^3 \right] \tag{34}$$

$$k_{ox} = \frac{2.9023 \cdot 10^{-6}}{A_{sf}} \cdot e^{\frac{3.9161 \cdot 10^5}{RT}} \tag{35}$$

Wang et al. (2022) implemented both the reduction and oxidation of ceria, and the kinetics was modelled using a two-step surface chemistry (a $H_2O$ adsorption/dissociation step and a charge-transfer step), coupled with the bulk-to-surface transport equilibrium (Zhao et al., 2016). Pan et al. (2020) considered the expression for the reduction kinetic from Bulfin et al. (2013), while the oxidation with $CO_2$ splitting reaction is implemented as an Arrhenius type equation with parameters provided by Le Gal et al. (2011). Orsini et al. (2024) implemented the same expression to model the reduction, while the $H_2O$-driven oxidation is described according to the apparent kinetic law obtained experimentally by Arifin and Weimer (2018) and transformed into a local kinetic law for the integration in the reactor model.

#### 3.2.3.3 Chemical modeling of alternative materials

Regarding the chemical modeling of alternative materials with respect to ceria, Wang et al. (2021) modelled the kinetics of reduction of the iron manganese oxide considering the reaction rate (Equation 36) proportional to a kinetic rate term, $\kappa(T)$ (Arrhenius equation), a reaction model, $f(\delta)$ (function of the reaction extent–Equation 37) and a pressure-dependent term, $h(p)$.

$$\frac{d\delta}{dt} = \kappa(T) \cdot f(\delta) \cdot h(p) = \left[ A_{red} e^{-\frac{E}{RT}} \right] \cdot f(\delta) \cdot \left[ 1 - \frac{p_{O_2}}{p_{O_2,eq}} \right]^{25.01} \tag{36}$$

$$f(\delta) = \begin{cases} 85.26 & 0 \le \delta < 0.05 \\ \dfrac{3(1-\delta)^{\frac{2}{3}}}{2\left[1-(1-\delta)^{\frac{1}{3}}\right]} & 0.05 \le \delta \le 1 \end{cases} \tag{37}$$

Several models that focused on nickel-ferrite oxides integrated the chemical reaction by considering both the kinetics of reduction and oxidation based on the Arrhenius-type expression. In particular, Villafán-Vidales et al. (2011) modelled the two steps considering $H_2O$ splitting in the oxidation phase (Equation 38 and (Equation 39), respectively), while Shu et al. (2021) integrated similar expressions for the $CO_2$-driven reaction.

$$r_{O_2} = k_{0,red} e^{-\frac{E_{red}}{RT}} \tag{38}$$

$$r_{H_2} = k_{0,ox} e^{-\frac{E_{ox}}{RT}} \tag{39}$$

Another approach is provided by Lange et al. (2015), in which the kinetics of reduction and $H_2O$-driven oxidation in the honeycomb structure is described as function of the maximum oxygen uptake capacity according to Agrafiotis et al. (2013).

A similar Arrhenius kinetics formulation was also integrated by Guene Lougou et al. (2023) to model the reaction of $CO_2$ splitting with $Co_3O_4$ and $CuFe_2O_4$ and by Martinek et al. (2014) with hercynite material ($H_2O$ splitting).

For what concerns examples of perovskite materials, Brendelberger et al. (2019b) modelled the reduction extent of $SrFeO_3$ according to the equilibrium expression provided in Equation 20, with the free parameters calibrated according to experimental measures. Recently, Zhao et al. (2025a), Zhao et al. (2025b) applied Equations 33–35 derived for ceria to model the reaction rates of Zr-doped ceria and lanthanum-based perovskites, updating only the thermodynamic properties as function of the non-stoichiometry depending on the material considered. Finally, the abovementioned work by Orsini et al. (2024) proposes a simple analytical methodology for using apparent kinetics data directly into space-dependent multiphysics reactor models, that is transversally applicable to any nonstoichiometric oxide, including perovskites. Kinetic studies of this kind are well established in the literature (Vyazovkin et al., 2011), with several works defining kinetic laws for chemical looping cycles using various oxygen carriers (Dai et al., 2016; Barde et al., 2016; Wenzel et al., 2017; Tang et al., 2021; Lu et al., 2018). This approach has also been applied to the ceria redox cycle (Lu et al., 2019), including the $CO_2$ (Farooqui et al., 2018) and $H_2O$ splitting steps (Arifin and Weimer, 2018). With this formulation, the reaction rate is expressed as factorized contributions accounting for the rate dependence on temperature, reaction progress (*i.e.*, solid conversion), and reactant concentration or partial pressure.

### 3.2.4 Radiative heat transfer modeling

The radiative heat transfer involves both the reaction chamber (surface-to-surface heat exchange) and the reactive element. Therefore, these two mechanisms need to be coupled to define the temperature field inside the redox material. Radiation represents another crucial phenomenon in the modeling of these systems, since the heat transfer in solar reactors operating above 1100 K is dominated by this mechanism (Wheeler et al., 2017). Redox materials are in general modelled as anisotropically

absorbing-scattering-emitting media according to the radiative heat transfer equation (RTE) reported in Equation 40. In this case, $\kappa$, $\alpha$, and $\beta$ are the scattering, absorption, and extinction coefficients, respectively, and for the geometric optic regime, the relation $\kappa + \alpha = \beta$ (Ackermann et al., 2017) holds. $\Phi$ represents the scattering phase function and $I = I(\mathbf{r}, \hat{\mathbf{s}}, t, \lambda)$ indicates the radiation intensity as function of position $\mathbf{r}$, direction of propagation $\hat{\mathbf{s}}$, time $t$, and wavelength $\lambda$. The subscript $b$ refers to the blackbody radiation, that is a function of the temperature. The integral over the solid angle $\Omega$ denotes the contribution of the radiation intensity over all the propagation directions.

$$\frac{1}{c}\cdot\frac{\partial I}{\partial t} + \hat{\mathbf{s}}\cdot\nabla I = -\beta I + \alpha I_b + \frac{\sigma}{4\pi}\int_{4\pi} I\Phi \mathrm{d}\Omega \tag{40}$$

The solution of Equation 40 allows to determine the radiative heat source term, $\nabla\cdot\mathbf{q}_{rad}$, that appears in the energy equation, according to Equation 41.

$$\nabla\cdot\mathbf{q}_{rad} = \alpha\left(4\pi I_b - \int_{4\pi} I \mathrm{d}\Omega\right) \tag{41}$$

The time-dependent term on the left-hand side is usually neglected, since its time scale variation is very small compared to the other processes involved in the reactor, such as the chemical reactions (Wheeler et al., 2017). The spectral and directional nature of the radiative equation imply additional challenges in the numerical solution of the model. For this reason, different approaches were proposed in the literature to solve the equation for an infinite angular resolution (Monte Carlo ray tracing, discrete ordinate, or finite volume methods), or simplify and discretize it to reduce the computational costs (Rosseland Diffusion approximation, P1 approximation) (Wheeler et al., 2017).

Monte Carlo ray tracing methods are one of the most exploited options in the literature thanks to their simplicity. Ackermann et al. (2017) and Wang et al. (2021) coupled the radiative heat transfer equation with a Monte Carlo ray tracing code that evaluates the radiative solar heat flux inside the reactor cavity, providing it to the multiphysics model as a boundary condition. The same approach has been followed by Furler and Steinfeld (2015), Zoller et al. (2019), and Wei et al. (2024), but with the significant difference of assuming the participating medium as isotropic. With this assumption, the scattering phase function $\Phi$ in the radiative heat transfer equation is assumed to be equal to one along all the propagating directions. Besides the solution of the RTE, Monte Carlo ray tracing methods are also widely adopted to solve the radiation outside the participating media and then coupled with other methods that focus specifically on the radiation in the participating media.

Zhang and Smith (2021), Bellan et al. (2019), and Sedighi et al. (2021) coupled the radiative heat transfer equation with a discrete ordinates model. With this method, Equation 40 for a given direction $\hat{\mathbf{s}}$ is transformed into a transport equation and solved with the same computational methods used for the fluid or energy equations. Sharma et al. (2023) followed the same approach, but a Monte Carlo ray tracing method based on the software Soltrace is also implemented to define the solar power distribution. The studies from Bala Chandran and Davidson (2016) and Valades-Pelayo et al. (2017) modelled the radiation inside the cavity with a Monte Carlo ray tracing method, while the radiative source term $\nabla\cdot\mathbf{q}_{rad}$ is obtained computing a finite volume method for unstructured mesh. The corresponding vector results from the discrete sum of the radiation intensity over $i$ angular directions, according to Equation 42.

$$\mathbf{q}_{rad} = \sum_i I\hat{\mathbf{s}}_i \tag{42}$$

Another approach often implemented in the literature is the Rosseland Diffusion Approximation (RDA). In this case, an approximate solution of the RTE is evaluated by defining an effective thermal conductivity with a cubic dependence on temperature that it is simply added in the thermal conduction term (Wheeler et al., 2017). This approximation can be applied only to porous structures with large enough extinction coefficients, resulting in large optical thickness (Keene et al., 2014). A comparison of the results obtained with this method and the exact solution computed with a Monte Carlo ray tracing method is provided by Lapp et al. (2013), indicating the possibility to accurately represent the radiation in optically thick mediums with less computational effort. With this approach, the radiative heat flux is modelled according to Equation 43, where $\beta_m$ is the Rosseland-mean extinction coefficient.

$$\mathbf{q}_{rad} = -k_{rad}\nabla T = -\frac{16\sigma T^3}{3\beta_m}\nabla T \tag{43}$$

Examples of this approach are provided by Orsini et al. (2024), Vega Puga et al. (2024), Brendelberger et al. (2020), Brendelberger (2024), Falter and Pitz-Paal (2018), Lapp and Lipiński (2014), and Keene et al. (2014). Lidor et al. (2021) and Lampe et al. (2025b) provided an example in which the RDA is coupled with the Beer-Lambert law for the volumetric absorption of the solar radiation. In the studies developed by Li et al. (2016), Martinek et al. (2014), Kyrimis et al. (2019), and Bader et al. (2015), the radiative heat transfer inside the porous receiver modelled with RDA was coupled with a Monte Carlo ray tracing model to trace the rays from the aperture of the cavity until they are absorbed in the reactive surfaces. Guene Lougou et al. (2018a) and Pan et al. (2018) proposed a model in which the RDA is coupled with the surface-to-surface heat transfer model provided by COMSOL Multiphysics® and based on the radiosity method. According to this approach, the radiosity of a given surface inside the reactor cavity is computed considering the total radiative heat flux leaving the surface element (Equation 44). In this case, $\sigma T^4$ is the blackbody emissive power, $F_{s-s'}$ is the view factor between surfaces $s$ and $s'$, while $\varepsilon_s$ and $J_s$ represent the emissivity and the global radiosity leaving the surface $s$, respectively.

$$J_s = (1-\varepsilon_s)G_s + \varepsilon_s\sigma T^4 = (1-\varepsilon_s)\int_{s-s'} F_{s-s'}J_{s'}\mathrm{d}s + \varepsilon_s\sigma T^4 \tag{44}$$

An alternative method to approximate the solution of the RTE for cases where the RDA is not applicable is represented by the modified differential approximate P1 model. Wang et al. (2022), Guene Lougou et al. (2023), Zhang et al. (2018), Shu et al. (2021), Villafán-Vidales et al. (2011), Dai and Haussener (2022), and Zhao et al. (2025a) applied this approach, where the radiative flux $\mathbf{q}_{rad}$ and the incident radiation $G_d$ are coupled according to Equation 45. As consequence, the radiative source term expression (Equation 41) can be rearranged as indicated in Equation 46 to obtain the irradiance $G$. This approximation does not require significantly higher computational costs, and it is considered to

be valid for porous media with optical thickness larger than 1 (Huang and Lin, 2021). On the other hand, it is important to mention that the described method is based on the assumption that the radiation intensity is scattered uniformly in all the directions (isotropic scattering media) (Guene Lougou et al., 2017c). If this is not the case and the radiation entering the reactor is collimated, a modified differential approximation is required (Villafán-Vidales et al., 2011).

$$\mathbf{q}_{\mathrm{rad}} = -\frac{1}{3\beta}\nabla G \tag{45}$$

$$\nabla \cdot \mathbf{q}_{\mathrm{rad}} = -\frac{1}{3\beta}\nabla^2 G = \alpha\left(4\pi I_{\mathrm{b}} - G\right) \tag{46}$$

Huang and Lin (2021), Guene Lougou et al. (2018b), and Scott et al. (2024) coupled the described P1 approximation model to solve the radiative equation in the porous media (participating domain) with the surface-to-surface model to obtain the radiation exchange inside the cavity (non-participating domain). Similarly, Cai et al. (2024) applied a Monte Carlo ray tracing method outside the participating media and the P1 approximation within it. A modified surface-to-surface method coupled with a Monte Carlo ray tracing code was used by Huang and Lin (2022) to evaluate the incident heat flux, while the P1 approximation method was implemented in the porous domain.

### 3.2.5 Modeling of redox material degradation

A central element in modeling solar thermochemical cycles is represented by the evaluation of the material degradation over multiple cycles. The strong temperature gradients have a significant impact on the optical performance of the components, decreasing their ability to efficiently transmit radiative power to the redox material (Vidal and Martinez, 2020). In addition, the redox material itself undergoes irreversible degradation during the performed chemical cycles, resulting in modified thermal and mechanical properties (Costa Oliveira et al., 2025). Although a precise evaluation of these phenomena over the life span of a solar reactor are of primary importance to evaluate the commercial feasibility of this technology, the integration of these considerations in multiphysics models is very limited. Zhao et al. (2025a) introduced degradation rates to account for the variation of optical performance and porosity over 30 years of operation. The annual porosity degradation rate has been assumed equal to 1%, while the annual optical performance degradation rate was indicated equal to 1.5% in line with the estimation of 0.65%–2% provided by specific studies on solar fields (Polo et al., 2025).

### 3.2.6 Focus on model validation

The multiphysics models described in the presented review differ in terms of type of reactor considered (*e.g.*, in terms of design or redox material used), as well as of modeling techniques implemented to describe the physical phenomena that occur in solar thermochemical reactors. As a direct consequence, an accurate validation of the models clarifying the range of validity for the proposed numerical analysis is of primary importance. In general, experimental validation of the proposed models is reported for a precise set of operating conditions or small variations of some key parameters. On the other hand, parametric analyses focusing on the discrepancy between numerical and experimental results under a wide range of operating conditions are limited. In addition, the prototype reactors that have been manufactured are mainly directly-irradiated of the cavity type with the redox material shaped as a single-scale (Wang et al., 2022; Furler and Steinfeld, 2015; Villafán-Vidales et al., 2011; Guene Lougou et al., 2018a; Rojas et al., 2025) or a dual-scale porosity structure (Zoller et al., 2022; Marxer et al., 2017; Schäppi et al., 2022; Ackermann et al., 2017). Experimental analyses on alternative reactor prototypes are limited to packed (Lanchi et al., 2013) or fluidized beds (Bellan et al., 2019), while innovative designs were not yet widely demonstrated.

Concerning the modeling of the chemical reaction, the range of applicability of the equilibrium assumption is analyzed by Venstrom et al. (2015) for the specific case of ceria implemented as redox material. The results indicate a good fit of the numerical model with the equilibrium assumption for what concerns the reduction step, while for the oxidation the approach maintains a good fit only below a given rate of oxidizing fluid ($CO_2$ for the mentioned study). Examples of comparison in terms of chemical reaction between models and experimental results are provided both assuming the equilibrium (Ackermann et al., 2017) or integrating the kinetics (Rojas et al., 2025; Wang et al., 2022).

In terms of heat transfer modeling, the two main approaches are represented by considering the solid redox material and the fluid as a unique phase solving only one energy equation (LTE approach) or by considering two separate phases coupling two energy equations together. The results from these two modeling approaches are compared by Zhang et al. (2018) and a direct relation between the temperature deviation and the velocity of the fluid inside the chamber is indicated. For both LTE (Furler and Steinfeld, 2015; Lanchi et al., 2013) and LTNE (Wang et al., 2022; Bellan et al., 2019; Villafán-Vidales et al., 2011; Ackermann et al., 2017) a large number of experimental validation studies is available in literature, providing the fit between numerical temperature profiles and real measurements. It is also important to mention how it has been proved that the numerical solution would strongly deviate from the experimental results by neglecting the heat losses on the boundaries of the reactor (Villafán-Vidales et al., 2011; Rojas et al., 2025).

Moving the attention to the radiative heat transfer modeling methodologies, a comparison between experimental measurements and numerical results is provided for models integrating Monte Carlo ray tracing codes (Ackermann et al., 2017), RDA (Guene Lougou et al., 2018a), and P1 approximation (Villafán-Vidales et al., 2011). In the mentioned cases, the temperature profile was analyzed. Experimental validation of the radiative flux distribution was instead reported by Furler and Steinfeld (Furler and Steinfeld, 2015). Finally, experimental validation was also reported for production rate profiles in time, in terms of oxygen evolution upon reduction (Ackermann et al., 2017; Orsini et al., 2024) or fuel evolution during oxidation (Orsini et al., 2024). In this case, however, a direct comparison against real measured data could require some more care, because of concomitant experimental effects including dispersion, mixing, and detector time lag inherent to the experimental apparatus and not to the splitting reaction chemistry (Orsini et al., 2024).

## 4 Summary and discussion

On a general perspective, the main assumptions applied in the proposed works are related to the physics implemented and the geometry considered in the model. In some of the analyzed studies, the fluid flow is not included in the analysis and a heat transfer model is applied to describe the system (Scott et al., 2024; Lapp and Lipiński, 2014; Zoller et al., 2019; Li et al., 2016). With this assumption, it is necessary to assume the concentration or the partial pressure of the gaseous species involved in the reaction imposed to a fixed value, neglecting the contribution of mass transfer mechanisms and pressure drops in the redox material. This assumption considers that the contribution of convection to the heat transfer is negligible, especially when working in vacuum conditions (Zoller et al., 2019). On the other hand, it was proved by other studies that integrating the fluid flow allows to consider the spatial variations in the $O_2$ partial pressure and the local thermal non-equilibrium in the porous medium, leading to a more accurate resolution of the nonstoichiometry field. In particular, the temperature difference between the solid and gas phases in the porous medium was proved to be significant due to the high irradiation magnitude (Wang et al., 2022; Dai and Haussener, 2022). It was suggested that, by avoiding a complete heat and mass transfer analysis, the estimation of the heat fluxes might deviate up to 15% (Lipiński et al., 2021). We shall also suspect that, in case of redox materials alternative to ceria exhibiting a larger oxygen release upon reduction, the deviation in accuracy experienced if the flow field is not solved could become even more pronounced. It is, thus, strongly suggested to always compare the simulation results with a full-physics implementation (within reasonable and feasible computation costs), especially when exploring novel reactor configurations, wide operational space, and novel oxygen carrier compositions. When the fluid flow was included in the model physics, a laminar regime was often assumed. It was previously reported how a turbulent flow could induce improved reaction rates in solar thermochemical applications (Wheeler et al., 2017), but this operational regime was rarely investigated and remains underexplored. At the same time, we recognize that some redox materials considered at present as promising (*e.g.*, perovskites) do suffer from a less favorable oxidation thermodynamics, and operating in a turbulent regime with relatively large oxidant flow rates–depending on the specific geometric configuration of the flow field and working principle of the reactor–could cause in general a further increase in the energy penalty. Such modeling extension on the fluid flow side could be worth to be explored–however, with some care concerning the optimal operating strategies and energy balance considerations around the reactor.

In addition, several studies provided multiphysics models without the integration of the chemistry of the reaction. In such cases, the analysis on the behavior of the temperature and velocity fields under various operating conditions was carried out, without considering the thermochemical performance of the system [SiC-based foam (Huang and Lin, 2021; Zhang et al., 2018), porous $NiFe_2O_4$ (Guene Lougou et al., 2018a), RPC structure (Cai et al., 2024), particles (Singh et al., 2017; Bellan et al., 2019; Sedighi et al., 2021)]. In these cases, the overestimation of the temperature field in the reduction step due to the neglected heat sink associated with the endothermic reaction is considered to be negligible (Singh et al., 2017). Another common simplification lies in considering a simplified geometry, developing 1D (Wang et al., 2022; Keene et al., 2014; Ackermann et al., 2017; Lidor et al., 2021; Dai and Haussener, 2022; Rojas et al., 2025) or 2D models (Lapp et al., 2013; Darfilal, 2020). In these cases, the represented system can differ from the reality, but at the same time, it is possible to easily develop a simulation tool with lower computational demand to test various designs and operating parameters (Brendelberger et al., 2019a).

For what concerns the design of the reactor, most of the models proposed in the literature focus on directly irradiated configurations of the cavity type. Studies that include an indirectly irradiated configuration are more limited and mainly associated to tubular configurations filled with reactive beds (packed or moving) of redox material instead of porous monoliths. Few multiphysics models of alternative designs, such as rotating or moving reactors, are available. More efforts in modeling novel reactor configurations would allow to explore accurately the performance boundaries of innovative solutions, while progressively establishing suitable numerical simulation techniques to advance research in this direction.

Regarding the redox material implemented, a porous monolith of ceria is by far the most common approach due to its benefit in terms of heat transfer mechanisms, available reactive surface, and chemical stability. In this context, the concept of dual-scale porosity proved to achieve better performance by enhancing the radiation absorption in the porous sample, as well as the oxidation kinetics. The chemical reaction of ceria is usually modelled by following two main approaches. In the first case, the fluid and solid phases are assumed to be in thermodynamic equilibrium and the redox reaction is assumed to be limited by heat transfer. This simplification has been proved to align well with experimental measures during the reduction step, while during oxidation the kinetics plays a bigger role. Consequently, generally the equilibrium assumption is applied to models that focus only on the reduction step, while assuming a complete re-oxidation of the material from its condition at the end of the same reduction. This approach is a valid alternative to benchmark the performance of a given configuration, but represents an overestimation of the results since during the oxidation phase additional energy inputs are required to run the process. Furthermore, operating conditions (*e.g.*, duration of the steps, flow rate of the oxidizing fluid) represent key parameters that might strongly influence the resulting performance. With the second approach, the kinetics of the reaction is integrated in the modeling framework, enabling a more accurate representation of the whole thermochemical cycle. In this case, the two steps are described according to analytical expressions valid for both the intermediate reactions, or separate correlations for oxygen and $H_2$/CO production rates. In both cases, the reaction process is assumed to be driven by singly or doubly ionized oxygen vacancies diffusion well described by Arrhenius-type equations, and expression for both $CO_2$ and $H_2O$ driven oxidation were provided. A small number of studies considered alternative redox material other than state-of-the-art ceria, with most of them focusing on ceramic structures coated with ferrite oxides of different nature. In this case, the equilibrium assumption represents a less accurate approach, since it was already proved

that alternative materials displayed a less favorable kinetics of reaction during the re-oxidation phase (Wei et al., 2023). For this reason, in all these studies, the complete reaction is modelled according to Arrhenius-type equations where the parameters are defined for each material to account for the kinetics of the reaction. Only few recent examples were found in which perovskites have been considered as redox material in space-dependent multiphysics reactor models (Zhao et al., 2025a; Zhao et al., 2025b). While thermodynamic 0D models can provide useful upper-bound efficiency estimates for perovskites, advancing toward higher-dimensional continuum-level reactor models is essential to capture spatial transport effects and finite-rate chemistry, thereby enabling more accurate performance predictions under realistic and material-specific operating conditions. Moreover, well-established and broadly applicable experimental techniques can be used to characterize the reaction chemistry, as they allow accurate extraction of kinetic parameters even for novel oxygen carrier compositions, followed by appropriate analytical methods for readily coupling such kinetics with space-dependent reactor models.

The radiative heat transfer is generally modelled by assuming the reactive material as a participating medium, and the radiative heat transfer equation is implemented by applying different methods for its solution. In some cases, the morphology of the material allows to consider it as an optically thick medium, applying simplifications to solve the radiative heat transfer with a lower computational cost. With this approach, the radiative heat flux inside the porous medium was often obtained by means of the Rosseland Diffusion Approximation (RDA) method or the P1 approximation. On the other hand, the rest of the reactor is generally modelled as a non-participating medium and the heat flux at each boundary is determined through Monte Carlo ray tracing methods. The fluid in the reaction chamber is commonly assumed transparent to the radiation. On the heat transfer side, the potentially large differences emerging in the thermophysical properties among different redox materials could have a non-negligible impact on the resulting process performance, especially in terms of material utilization distribution in space-dependent numerical predictions, and should not be overlooked.

## 5 Conclusion

The literature review presented in this paper focuses on the multiphysics modeling of non-volatile and non-stoichiometric two-step solar thermochemical cycles, which represent the most promising and most studied state-of-the-art option for this application. The differences between the available works in terms of reactor design and modeling approaches of the main physical phenomena of the cycle (namely: fluid flow, heat transfer, and solid-gas chemical reactions) were summarized and discussed. For what concerns the modeling of heat and mass transfer mechanisms, most of the works followed the same approaches by assuming a laminar flow and considering a local thermal non-equilibrium between the solid and gas phase in the reactive porous medium. On the other hand, a wide range of possibilities based on different assumptions is provided for what regards the modeling of the solid-gas chemical reaction and radiative heat transfer.

Despite the numerous studies available on these systems, an important research gap was identified in the few numbers of models describing the integration of alternative materials other than ceria. Innovative oxygen carriers, such as perovskites, were suggested as potentially valid candidates to enhance the performance of such reactors, but the limited number of studies that accurately characterize their properties (*e.g.*, thermochemical, thermophysical, or radiative), as well as the uncertainty concerning their high-performance potential in realistic operating conditions against idealized laboratory conditions, are likely limiting factors currently to their massive multiphysics modeling investigation in actual reactor concepts. In addition, many of the models available consider cavity-type directly irradiated reactors, and innovative approaches, such as designs involving a moving redox material, are less represented. In particular, heat recovery systems are indicated to be a promising route to improve the performance, but few models have integrated similar approaches so far. Future advancements in the field should move towards the application of the well-established modeling techniques described in this paper on alternative reactor designs and redox materials, in order to benchmark their impact with respect to the main limitations of state-of-the-art configurations.

Overall, we report a wide overview of the state-of-the-art multiphysics modeling for two-step solar thermochemical fuel production systems, while summarizing the main gaps identified in the literature and providing useful guidelines to advance the research in this direction.

## Author contributions

MR: Data curation, Writing – original draft, Methodology, Formal Analysis, Validation, Investigation, Visualization, Conceptualization. FO: Validation, Writing – review and editing, Conceptualization, Methodology, Supervision, Investigation. DF: Validation, Methodology, Conceptualization, Supervision, Investigation, Funding acquisition, Writing – review and editing. MS: Funding acquisition, Writing – review and editing, Supervision, Methodology, Conceptualization, Validation.

## Funding

The authors declare that financial support was received for the research and/or publication of this article. This publication is part of the project NODES which has received funding from the MUR–M4C2 1.5 of PNRR funded by the European Union - NextGenerationEU (Grant agreement no. ECS00000036). H2SHIFT project - Horizon Europe project, ID 101137953.

## Conflict of interest

The authors declare that the research was conducted in the absence of any commercial or financial relationships that could be construed as a potential conflict of interest.

## Generative AI statement

The authors declare that no Generative AI was used in the creation of this manuscript.

Any alternative text (alt text) provided alongside figures in this article has been generated by Frontiers with the support of artificial intelligence and reasonable efforts have been made to ensure accuracy, including review by the authors wherever possible. If you identify any issues, please contact us.

## Publisher's note



## References

Abedini Najafabadi, H., and Ozalp, N. (2018). An advanced modeling and experimental study to improve temperature uniformity of a solar receiver. *Energy* 165, 984–998. doi:10.1016/j.energy.2018.10.033

Ackermann, S., Scheffe, J. R., Duss, J., and Steinfeld, A. (2014). Morphological characterization and effective thermal conductivity of dual-scale reticulated porous structures. *Materials* 7 (11), 7173–7195. doi:10.3390/ma7117173

Ackermann, S., Takacs, M., Scheffe, J., and Steinfeld, A. (2017). Reticulated porous ceria undergoing thermochemical reduction with high-flux irradiation. *Int. J. Heat Mass Transf.* 107, 439–449. doi:10.1016/j.ijheatmasstransfer.2016.11.032

Agrafiotis, C., Zygogianni, A., Pagkoura, C., Kostoglou, M., and Konstandopoulos, A. G. (2013). Hydrogen production *via* solar-aided water splitting thermochemical cycles with nickel ferrite: experiments and modeling. *AIChE J.* 59 (4), 1213–1225. doi:10.1002/aic.13882

Al-Shankiti, I. A., Bayon, A., and Weimer, A. W. (2020). Reduction kinetics of hercynite redox materials for solar thermochemical water splitting. *Chem. Eng. J.* 389, 124429. doi:10.1016/j.cej.2020.124429

Alonso, E., and Romero, M. (2015). A directly irradiated solar reactor for kinetic analysis of non-volatile metal oxides reductions. *Int. J. Energy Res.* 39 (9), 1217–1228. doi:10.1002/er.3320

Arifin, D., and Weimer, A. W. (2018). Kinetics and mechanism of solar-thermochemical H2 and CO production by oxidation of reduced CeO2. *Sol. Energy* 160, 178–185. doi:10.1016/j.solener.2017.11.075

Bader, R., Bala Chandran, R., Venstrom, L. J., Sedler, S. J., Krenzke, P. T., De Smith, R. M., et al. (2015). Design of a solar reactor to split CO2 *via* isothermal redox cycling of ceria. *J. Sol. Energy Eng.* 137, 031007. doi:10.1115/1.4028917

Bala Chandran, R., and Davidson, J. H. (2016). Model of transport and chemical kinetics in a solar thermochemical reactor to split carbon dioxide. *Chem. Eng. Sci.* 146, 302–315. doi:10.1016/j.ces.2016.03.001

Bala Chandran, R., De Smith, R. M., and Davidson, J. H. (2015). Model of an integrated solar thermochemical reactor/reticulated ceramic foam heat exchanger for gas-phase heat recovery. *Int. J. Heat Mass Transf.* 81, 404–414. doi:10.1016/j.ijheatmasstransfer.2014.10.053

Barde, A. A., Klausner, J. F., and Mei, R. (2016). Solid state reaction kinetics of iron oxide reduction using hydrogen as a reducing agent. *Int. J. Hydrogen Energy* 41 (24), 10103–10119. doi:10.1016/j.ijhydene.2015.12.129

Barone, G., Buonomano, A., Forzano, C., Giuzio, G. F., and Palombo, A. (2023). Energy performance assessment of a solar-driven thermochemical cycle device for green hydrogen production. *Sustain. Energy Technol. Assessments* 60, 103463. doi:10.1016/j.seta.2023.103463

Bayer Botero, N., Thomey, D., Guerra Niehoff, A., Roeb, M., Sattler, C., and Pitz-Paal, R. (2016). Modelling and scaling analysis of a solar reactor for sulphuric acid cracking in a hybrid sulphur cycle process for thermochemical hydrogen production. *Int. J. Hydrogen Energy* 41 (19), 8008–8019. doi:10.1016/j.ijhydene.2015.11.088

Bellan, S., Alonso, E., Gomez-Garcia, F., Perez-Rabago, C., Gonzalez-Aguilar, J., and Romero, M. (2013). Thermal performance of lab-scale solar reactor designed for kinetics analysis at high radiation fluxes. *Chem. Eng. Sci.* 101, 81–89. doi:10.1016/j.ces.2013.06.033

Bellan, S., Saurez, C. C., Gonzalez-Aguilar, J., and Romero, M. (2014a). "Numerical study of a beam-down solar thermochemical reactor for chemical kinetics analysis," in *Presented at the ASME 2014 8th international conference on energy sustainability collocated with the ASME 2014 12th international conference on fuel cell science, engineering and technology*. American Society of Mechanical Engineers Digital Collection. doi:10.1115/ES2014-6573

Bellan, S., Alonso, E., Perez-Rabago, C., Gonzalez-Aguilar, J., and Romero, M. (2014b). Numerical modeling of solar thermochemical reactor for kinetic analysis. *Energy Procedia* 49, 735–742. doi:10.1016/j.egypro.2014.03.079

Bellan, S., Matsubara, K., Cho, H. S., Gokon, N., and Kodama, T. (2018a). CFD-DEM investigation on flow and temperature distribution of ceria particles in a beam-down fluidized bed reactor. *AIP Conf. Proc.* 2033 (1), 130003. doi:10.1063/1.5067137

Bellan, S., Matsubara, K., Cho, H. S., Gokon, N., and Kodama, T. (2018b). A CFD-DEM study of hydrodynamics with heat transfer in a gas-solid fluidized bed reactor for solar thermal applications. *Int. J. Heat Mass Transf.* 116, 377–392. doi:10.1016/j.ijheatmasstransfer.2017.09.015

Bellan, S., Kodama, T., Matsubara, K., Gokon, N., Cho, H. S., and Inoue, K. (2019). Heat transfer and particulate flow analysis of a 30 kW directly irradiated solar fluidized bed reactor for thermochemical cycling. *Chem. Eng. Sci.* 203, 511–525. doi:10.1016/j.ces.2018.09.012

Bellan, S., Kodama, T., Seok Cho, H., and Kim, J.-S. (2022). Hydrogen production by solar fluidized bed reactor using ceria: euler-lagrange modelling of gas-solid flow to optimize the internally circulating fluidized bed. *J. Therm. Sci. Technol.* 17 (2), 22-00076–00076. doi:10.1299/jtst.22-00076

Brendelberger, S. (2024). R2Mx plant model for solar thermochemical hydrogen production at MW scale. *Int. J. Hydrogen Energy* 91, 1407–1421. doi:10.1016/j.ijhydene.2024.10.050

Brendelberger, S., Holzemer-Zerhusen, P., von Storch, H., and Sattler, C. (2019a). Performance assessment of a heat recovery system for monolithic receiver-reactors. *J. Sol. Energy Eng.* 141 (2), 021008. doi:10.1115/1.4042241

Brendelberger, S., Vieten, J., Roeb, M., and Sattler, C. (2019b). Thermochemical oxygen pumping for improved hydrogen production in solar redox cycles. *Int. J. Hydrogen Energy* 44 (20), 9802–9810. doi:10.1016/j.ijhydene.2018.12.135

Brendelberger, S., Rosenstiel, A., Lopez-Roman, A., Prieto, C., and Sattler, C. (2020). Performance analysis of operational strategies for monolithic receiver-reactor arrays in solar thermochemical hydrogen production plants. *Int. J. Hydrogen Energy* 45 (49), 26104–26116. doi:10.1016/j.ijhydene.2020.06.191

Brendelberger, S., Holzemer-Zerhusen, P., Vega Puga, E., Roeb, M., and Sattler, C. (2022). Study of a new receiver-reactor cavity system with multiple Mobile redox units for solar thermochemical water splitting. *Sol. Energy* 235, 118–128. doi:10.1016/j.solener.2022.02.013

Bulfin, B., Lowe, A. J., Keogh, K. A., Murphy, B. E., Lübben, O., Krasnikov, S. A., et al. (2013). Analytical model of CeO2 oxidation and reduction. *J. Phys. Chem. C* 117 (46), 24129–24137. doi:10.1021/jp406578z

Bulfin, B., Hoffmann, L., de Oliveira, L., Knoblauch, N., Call, F., Roeb, M., et al. (2016). Statistical thermodynamics of non-stoichiometric ceria and ceria zirconia solid solutions. *Phys. Chem. Chem. Phys.* 18 (33), 23147–23154. doi:10.1039/C6CP03158G

Bulfin, B., Vieten, J., Agrafiotis, C., Roeb, M., and Sattler, C. (2017). Applications and limitations of two step metal oxide thermochemical redox cycles; a review. *J. Mater. Chem. A* 5 (36), 18951–18966. doi:10.1039/C7TA05025A

Cai, B. (2024). "Numerical simulation study on solar-driven CeO2 reduction reaction," in *2024 4th international conference on energy, power and electrical engineering (EPEE), Sept*, 1318–1321. doi:10.1109/EPEE63731.2024.10875182

Carrillo, R. J., and Scheffe, J. R. (2017). Advances and trends in redox materials for solar thermochemical fuel production. *Sol. Energy* 156, 3–20. doi:10.1016/j.solener.2017.05.032

Corgnale, C., Ma, Z., and Shimpalee, S. (2019). Modeling of a direct solar receiver reactor for decomposition of sulfuric acid in thermochemical hydrogen production cycles. *Int. J. Hydrogen Energy* 44 (50), 27237–27247. doi:10.1016/j.ijhydene.2019.08.231

Costa Oliveira, F. A., Sardinha, M., Netto, J. M. J., Farinha, M., Leite, M., Barreiros, M. A., et al. (2025). Mechanical performance of ceria-coated 3D-Printed black zirconia cellular structures after solar thermochemical CO/H2 fuel production cycles. *Crystals* 15 (7), 629. doi:10.3390/cryst15070629

Dai, X., and Haussener, S. (2022). Non-uniform porous structures and cycling control for optimized fixed-bed solar thermochemical water splitting. *J. Sol. Energy Eng.* 144, 030904. doi:10.1115/1.4052960

Dai, X., Cheng, J., Li, Z., Liu, M., Ma, Y., and Zhang, X. (2016). Reduction kinetics of lanthanum ferrite perovskite for the production of synthesis gas by chemical-looping methane reforming. *Chem. Eng. Sci.* 153, 236–245. doi:10.1016/j.ces.2016.07.011

Darfilal, D. (2020). Solar hydrogen production by thermochemical reaction: development of a packed-bed reactor. *J. Therm. Eng.* 6 (2), 152–169. doi:10.18186/thermal.729318

Davenport, T. C., Yang, C.-K., Kucharczyk, C. J., Ignatowich, M. J., and Haile, S. M. (2016). Maximizing fuel production rates in isothermal solar thermochemical fuel production. *Appl. Energy* 183, 1098–1111. doi:10.1016/j.apenergy.2016.09.012

de la Calle, A., and Bayon, A. (2019). Annual performance of a thermochemical solar syngas production plant based on non-stoichiometric CeO2. *Int. J. Hydrogen Energy* 44 (3), 1409–1424. doi:10.1016/j.ijhydene.2018.11.076

Ermanoski, I., Siegel, N. P., and Stechel, E. B. (2013). A new reactor concept for efficient solar-thermochemical fuel production. *J. Sol. Energy Eng.* 135, 031002. doi:10.1115/1.4023356

Ezbiri, M., Takacs, M., Theiler, D., Michalsky, R., and Steinfeld, A. (2017). Tunable thermodynamic activity of $La_x Sr_{1-x} Mn_y Al_{1-y} O_{3-\delta}$ ($0 \le x \le 1$, $0 \le y \le 1$) perovskites for solar thermochemical fuel synthesis. *J. Mater. Chem. A* 5 (8), 4172–4182. doi:10.1039/C6TA06644E

Falter, C. P., and Pitz-Paal, R. (2018). Modeling counter-flow particle heat exchangers for two-step solar thermochemical syngas production. *Appl. Therm. Eng.* 132, 613–623. doi:10.1016/j.applthermaleng.2017.12.087

Farooqui, A. E., Pica, A. M., Marocco, P., Ferrero, D., Lanzini, A., Fiorilli, S., et al. (2018). Assessment of kinetic model for ceria oxidation for chemical-looping CO2 dissociation. *Chem. Eng. J.* 346, 171–181. doi:10.1016/j.cej.2018.04.041

Furler, P., and Steinfeld, A. (2015). Heat transfer and fluid flow analysis of a 4 kW solar thermochemical reactor for Ceria redox cycling. *Chem. Eng. Sci.* 137, 373–383. doi:10.1016/j.ces.2015.05.056

Gager, E., Frye, M., McCord, D., Scheffe, J., and Nino, J. C. (2022). Reticulated porous lanthanum strontium manganite structures for solar thermochemical hydrogen production. *Int. J. Hydrogen Energy* 47 (73), 31152–31164. doi:10.1016/j.ijhydene.2022.07.052

Getahun Dessie, Y., Guene Lougou, B., Hong, Q., Heping, T., Juqi, Z., Baohai, G., et al. (2020). Thermal performance analysis of a solar reactor designed for syngas production. *Energies* 13 (13), 3405. doi:10.3390/en13133405

Grobbel, J., Brendelberger, S., Sattler, C., and Pitz-Paal, R. (2017). Heat transfer in a directly irradiated ceria particle bed under vacuum conditions. *Sol. Energy* 158, 737–745. doi:10.1016/j.solener.2017.10.022

Grobbel, J., Pitz-Paal, R., and Kruggel-Emden, H. (2019). *Modeling solar particle receivers with the discrete element method*. Aachen, Germany: RWTH Aachen University.

Guene Lougou, B., Hong, J., Shuai, Y., Huang, X., Yuan, Y., and Tan, H. (2017a). Production mechanism analysis of H2 and CO *via* solar thermochemical cycles based on iron oxide (Fe3O4) at high temperature. *Sol. Energy* 148, 117–127. doi:10.1016/j.solener.2017.03.050

Guene Lougou, B., Shuai, Y., Xing, H., Yuan, Y., and Tan, H. (2017b). Thermal performance analysis of solar thermochemical reactor for syngas production. *Int. J. Heat Mass Transf.* 111, 410–418. doi:10.1016/j.ijheatmasstransfer.2017.04.007

Guene Lougou, B., Shuai, Y., Chen, X., Yuan, Y., Tan, H., and Xing, H. (2017c). Analysis of radiation heat transfer and temperature distributions of solar thermochemical reactor for syngas production. *Front. Energy* 11 (4), 480–492. doi:10.1007/s11708-017-0506-2

Guene Lougou, B., Shuai, Y., Pan, R., Chaffa, G., and Tan, H. (2018a). Heat transfer and fluid flow analysis of porous medium solar thermochemical reactor with quartz glass cover. *Int. J. Heat Mass Transf.* 127, 61–74. doi:10.1016/j.ijheatmasstransfer.2018.06.153

Guene Lougou, B., Shuai, Y., Pan, R., Chaffa, G., Ahouannou, C., Zhang, H., et al. (2018b). Radiative heat transfer and thermal characteristics of Fe-based oxides coated SiC and alumina RPC structures as integrated solar thermochemical reactor. *Sci. China Technol. Sci.* 61 (12), 1788–1801. doi:10.1007/s11431-018-9294-y

Guene Lougou, B., Han, D., Zhang, H., Jiang, B., Anees, J., Ahouannou, C., et al. (2020). Numerical and experimental analysis of reactor optimum design and solar thermal-chemical energy conversion for multidisciplinary applications. *Energy Convers. Manag.* 213, 112870. doi:10.1016/j.enconman.2020.112870

Guene Lougou, B., Wu, L., Ma, D., Geng, B., Jiang, B., Han, D., et al. (2023). Efficient conversion of solar energy through a macroporous ceramic receiver coupling heat transfer and thermochemical reactions. *Energy* 271, 126989. doi:10.1016/j.energy.2023.126989

Guo, Y., Chen, J., Song, H., Zheng, K., Wang, J., Wang, H., et al. (2024). A review of solar thermochemical cycles for fuel production. *Appl. Energy* 357, 122499. doi:10.1016/j.apenergy.2023.122499

Haeussler, A., Abanades, S., Jouannaux, J., and Julbe, A. (2018). Non-stoichiometric redox active perovskite materials for solar thermochemical fuel production: a review. *Catalysts* 8, 611. doi:10.3390/catal8120611

Haeussler, A., Abanades, S., Julbe, A., Jouannaux, J., Drobek, M., Ayral, A., et al. (2020a). Remarkable performance of microstructured ceria foams for thermochemical splitting of H2O and CO2 in a novel high–temperature solar reactor. *Chem. Eng. Res. Des.* 156, 311–323. doi:10.1016/j.cherd.2020.02.008

Haeussler, A., Abanades, S., Julbe, A., Jouannaux, J., and Cartoixa, B. (2020b). Solar thermochemical fuel production from H2O and CO2 splitting *via* two-step redox cycling of reticulated porous ceria structures integrated in a monolithic cavity-type reactor. *Energy* 201, 117649. doi:10.1016/j.energy.2020.117649

Haeussler, A., Abanades, S., Julbe, A., Jouannaux, J., and Cartoixa, B. (2020c). Two-step CO2 and H2O splitting using perovskite-coated ceria foam for enhanced green fuel production in a porous volumetric solar reactor. *J. CO2 Util.* 41, 101257. doi:10.1016/j.jcou.2020.101257

Hao, Y., Yang, C.-K., and Haile, S. M. (2014). Ceria–zirconia solid solutions ($Ce_{1-x}Zr_xO_{2-\delta}$, $x \le 0.2$) for solar thermochemical water splitting: a thermodynamic study. *Chem. Mater.* 26 (20), 6073–6082. doi:10.1021/cm503131p

Hathaway, B. J., Bala Chandran, R., Sedler, S., Thomas, D., Gladen, A., Chase, T., et al. (2015). Effect of flow rates on operation of a solar thermochemical reactor for splitting CO2 *via* the isothermal Ceria redox cycle. *J. Sol. Energy Eng.* 138, 011007. doi:10.1115/1.4032019

Huang, H., and Lin, M. (2021). Optimization of solar receivers for high-temperature solar conversion processes: direct vs. indirect illumination designs. *Appl. Energy* 304, 117675. doi:10.1016/j.apenergy.2021.117675

Huang, H., and Lin, M. (2022). Dynamic behavior of solar thermochemical reactors for fuel generation: modeling and control strategies. *Energy Convers. Manag.* 270, 116232. doi:10.1016/j.enconman.2022.116232

Huang, X., Lin, Y., Yao, X., Liu, Y., Gao, F., and Zhang, H. (2024). Thermal stress mechanism of thermochemical reactor of 5 kW solar simulator with temperature distribution as the load condition. *Processes* 12 (5), 1016. doi:10.3390/pr12051016

Jia, J., Seitz, L. C., Benck, J. D., Huo, Y., Chen, Y., Ng, J. W. D., et al. (2016). Solar water splitting by photovoltaic-electrolysis with a solar-to-hydrogen efficiency over 30%. *Nat. Commun.* 7 (1), 13237. doi:10.1038/ncomms13237

Keene, D. J., Lipiński, W., and Davidson, J. H. (2014). The effects of morphology on the thermal reduction of nonstoichiometric ceria. *Chem. Eng. Sci.* 111, 231–243. doi:10.1016/j.ces.2014.01.010

Kim, S. J., and Jang, S. P. (2002). Effects of the darcy number, the prandtl number, and the reynolds number on local thermal non-equilibrium. *Int. J. Heat Mass Transf.* 45 (19), 3885–3896. doi:10.1016/S0017-9310(02)00109-6

Kopping, S. J., Hoeniges, J., Greenhagen, J., Matejczyk, Z., and Venstrom, L. J. (2019). Model of the solar-driven reduction of cobalt oxide in a particle suspension reactor. *Sol. Energy* 177, 713–723. doi:10.1016/j.solener.2018.11.057

Kyrimis, S., Le Clercq, P., and Brendelberger, S. (2019). 3D modelling of a solar thermochemical reactor for MW scaling-up studies. *AIP Conf. Proc.* 2126 (1), 180013. doi:10.1063/1.5117693

Lou, J., Lu, X., Wu, Y., Tian, Z., Liu, L., Zhou, X., et al. (2024). Thermodynamic evaluation of nonstoichiometric oxides for efficient and practical solar thermochemical hydrogen production. *Energy Convers. Manag.* 314, 118156. doi:10.1016/j.enconman.2024.118156

Lampe, J., and Menz, S. (2024). Optimized operational strategy of a solar reactor for thermochemical hydrogen generation. *Optim. Eng.* 25 (1), 29–61. doi:10.1007/s11081-023-09855-3

Lampe, J., Krause, J., and Menz, S. (2025a). Process behavior analysis of a fixed-bed solar reactor for hydrogen generation *via* two-step thermochemical redox cycling. *Int. J. Hydrogen Energy* 144, 1328–1342. doi:10.1016/j.ijhydene.2025.03.114

Lampe, J., Henke, S., Menz, S., and Fend, T. (2025b). Solar-driven thermochemical water splitting: 3D energy flow analysis of a volumetric fixed-bed reactor design. *Int. J. Hydrogen Energy* 104, 584–598. doi:10.1016/j.ijhydene.2024.08.386

Lanchi, M., Varsano, F., Brunetti, B., Murmura, M. A., Annesini, M. C., Turchetti, L., et al. (2013). Thermal characterization of a cavity receiver for hydrogen production by thermochemical cycles operating at moderate temperatures. *Sol. Energy* 92, 256–268. doi:10.1016/j.solener.2013.03.008

Lange, M., Roeb, M., Sattler, C., and Pitz-Paal, R. (2015). Efficiency assessment of a two-step thermochemical water-splitting process based on a dynamic process model. *Int. J. Hydrogen Energy* 40 (36), 12108–12119. doi:10.1016/j.ijhydene.2015.07.056

Lapp, J., and Lipiński, W. (2014). Transient three-dimensional heat transfer model of a solar thermochemical reactor for H2O and CO2 splitting *via* nonstoichiometric Ceria redox cycling. *J. Sol. Energy Eng.* 136, 031006. doi:10.1115/1.4026465

Lapp, J., Davidson, J. H., and Lipiński, W. (2013). Heat transfer analysis of a solid-solid heat recuperation system for solar-driven nonstoichiometric redox cycles. *J. Sol. Energy Eng.* 135, 031004. doi:10.1115/1.4023357

Le Gal, A., Abanades, S., and Flamant, G. (2011). CO2 and H2O splitting for thermochemical production of solar fuels using nonstoichiometric ceria and ceria/zirconia solid solutions. *Energy Fuels* 25 (10), 4836–4845. doi:10.1021/ef200972r

Li, L., Chen, C., Singh, A., Rahmatian, N., AuYeung, N., Randhir, K., et al. (2016). A transient heat transfer model for high temperature solar thermochemical reactors. *Int. J. Hydrogen Energy* 41 (4), 2307–2325. doi:10.1016/j.ijhydene.2015.11.079

Li, S., Wheeler, V. M., Kreider, P. B., Bader, R., and Lipiński, W. (2018). Thermodynamic analyses of fuel production *via* solar-driven non-stoichiometric metal oxide redox cycling. Part 2. Impact of solid–gas flow configurations and active material composition on system-level efficiency. *Energy Fuels* 32 (10), 10848–10863. doi:10.1021/acs.energyfuels.8b02082

Li, S., Wheeler, V. M., Kumar, A., and Lipiński, W. (2020). Numerical modelling of ceria undergoing reduction in a particle–gas counter-flow: effects of chemical kinetics under isothermal conditions. *Chem. Eng. Sci.* 218, 115553. doi:10.1016/j.ces.2020.115553

Li, S., Wheeler, V. M., Kumar, A., Venkataraman, M. B., Muhich, C. L., Hao, Y., et al. (2022). Thermodynamic guiding principles for designing nonstoichiometric redox materials for solar thermochemical fuel production: ceria, perovskites, and beyond. *Energy Tech.* 10 (1), 2000925. doi:10.1002/ente.202000925

Lidor, A., and Bulfin, B. (2024). A critical perspective and analysis of two-step thermochemical fuel production cycles. *Sol. Compass* 11, 100077. doi:10.1016/j.solcom.2024.100077

Lidor, A., Fend, T., Roeb, M., and Sattler, C. (2021). High performance solar receiver–reactor for hydrogen generation. *Renew. Energy* 179, 1217–1232. doi:10.1016/j.renene.2021.07.089

Lin, M., and Haussener, S. (2015). Solar fuel processing efficiency for Ceria redox cycling using alternative oxygen partial pressure reduction methods. *Energy* 88, 667–679. doi:10.1016/j.energy.2015.06.006

Lipiński, W., Abbasi-Shavazi, E., Chen, J., Coventry, J., Hangi, M., Iyer, S., et al. (2021). Progress in heat transfer research for high-temperature solar thermal applications. *Appl. Therm. Eng.* 184, 116137. doi:10.1016/j.applthermaleng.2020.116137

Long, Y., Jiao, F., Yang, S., Weng, Y., and Liu, Q. (2024). A novel exergy analysis method for cerium-based solar thermochemical cycles. *Appl. Energy* 373, 123875. doi:10.1016/j.apenergy.2024.123875

Lou, J., Tian, Z., Wu, Y., Li, X., Qian, X., Haile, S. M., et al. (2022). Thermodynamic assessment of nonstoichiometric oxides for solar thermochemical fuel production. *Sol. Energy* 241, 504–514. doi:10.1016/j.solener.2022.05.008

Lu, C., Li, K., Wang, H., Zhu, X., Wei, Y., Zheng, M., et al. (2018). Chemical looping reforming of methane using magnetite as oxygen carrier: structure evolution and reduction kinetics. *Appl. Energy* 211, 1–14. doi:10.1016/j.apenergy.2017.11.049

Lu, Y., Zhu, L., Agrafiotis, C., Vieten, J., Roeb, M., and Sattler, C. (2019). Solar fuels production: two-step thermochemical cycles with cerium-based oxides. *Prog. Energy Combust. Sci.* 75, 100785. doi:10.1016/j.pecs.2019.100785

Ma, T. T., Zhu, Y. Z., Chen, H. J., Ma, Y., and Yang, L. (2015). Simulation on a novel solar high-temperature thermochemical coupled phase-change reactor. *Energy Procedia* 69, 471–480. doi:10.1016/j.egypro.2015.03.054

Ma, T., Fu, M., Cong, J., Zhang, X., Zhang, Q., Sayfieva, K. F., et al. (2024). Analysis of heat and mass transfer in a porous solar thermochemical reactor. *Energy* 294, 130842. doi:10.1016/j.energy.2024.130842

Martinek, J., Viger, R., and Weimer, A. W. (2014). Transient simulation of a tubular packed bed solar receiver for hydrogen generation *via* metal oxide thermochemical cycles. *Sol. Energy* 105, 613–631. doi:10.1016/j.solener.2014.04.022

Marxer, D., Furler, P., Takacs, M., and Steinfeld, A. (2017). Solar thermochemical splitting of CO2 into separate streams of CO and O2 with high selectivity, stability, conversion, and efficiency. *Energy Environ. Sci.* 10, 1142–1149. doi:10.1039/C6EE03776C

Menz, S., Lampe, J., Seeger, T., and Henke, S. (2023). Physical system behavior and energy flow analysis of a solar driven hydrogen production plant based on two-step thermochemical redox cycles. *Int. J. Hydrogen Energy* 48 (96), 37564–37578. doi:10.1016/j.ijhydene.2023.06.112

Mohite, S. J., and Reddy, K. S. (2023). Optical and thermal analysis of solar parabolic dish cavity receiver system for hydrogen production using deep learning. *Energy Convers. Manag.* 292, 117415. doi:10.1016/j.enconman.2023.117415

Moretti, C., Patil, V., Falter, C., Geissbühler, L., Patt, A., and Steinfeld, A. (2023). Technical, economic and environmental analysis of solar thermochemical production of drop-in fuels. *Sci. Total Environ.* 901, 166005. doi:10.1016/j.scitotenv.2023.166005

Muhich, C. L., Blaser, S., Hoes, M. C., and Steinfeld, A. (2018). Comparing the solar-to-fuel energy conversion efficiency of ceria and perovskite based thermochemical redox cycles for splitting H2O and CO2. *Int. J. Hydrogen Energy* 43 (41), 18814–18831. doi:10.1016/j.ijhydene.2018.08.137

Oberkirsch, L., Grobbel, J., Maldonado Quinto, D., Schwarzbözl, P., and Hoffschmidt, B. (2022). Controlling a solar receiver with multiple thermochemical reactors for hydrogen production by an LSTM neural network based Cascade controller. *Sol. Energy* 243, 483–493. doi:10.1016/j.solener.2022.08.007

Oles, A. S., and Jackson, G. S. (2015). Modeling of a concentrated-solar, falling-particle receiver for ceria reduction. *Sol. Energy* 122, 126–147. doi:10.1016/j.solener.2015.08.009

Onigbajumo, A., Swarnkar, P., Will, G., Sundararajan, T., Taghipour, A., Couperthwaite, S., et al. (2022). Techno-economic evaluation of solar-driven ceria thermochemical water-splitting for hydrogen production in a fluidized bed reactor. *J. Clean. Prod.* 371, 133303. doi:10.1016/j.jclepro.2022.133303

Ophoff, C., Ozalp, N., and Moens, D. (2020). Monte carlo ray tracing-coupled computational fluid dynamic modeling and experimental testing of a 1-kW solar cavity receiver radiated *via* 7-kW HFSS. *J. Sol. Energy Eng.* 142, 061003. doi:10.1115/1.4046779

Orsini, F., Ferrero, D., Papurello, D., and Santarelli, M. (2024). Solar thermochemical fuel production: a novel, validated multiphysics reactor model for the reduction–oxidation of nonstoichiometric redox cycles.

Pan, R., Lougou, B. G., Shuai, Y., Zhang, G., and Zhang, H. (2018). Heat transfer modeling of a high-temperature porous-medium filled solar thermochemical reactor for hydrogen and synthesis gas production. *J. Heat Transf.* 141, 022601. doi:10.1115/1.4041707

Pan, H., Lu, Y., and Zhu, L. (2020). Numerical modeling of CO2 splitting in high-temperature solar-driven oxygen permeation membrane reactors. *J. Sol. Energy Eng.* 143, 021001. doi:10.1115/1.4048014

Pan, H., Zhao, Y., Wang, Z., Lu, Y., and Li, Y. (2024). The study of CO2 splitting kinetics on LSM perovskite oxides in the solar-driven two-step thermochemical cycle. *Appl. Catal. A General* 672, 119591. doi:10.1016/j.apcata.2024.119591

Panlener, R. J. (2025). A thermodynamic study of nonstoichiometric cerium dioxide. *J. Phys. Chem. Solids* 36 (11). doi:10.1016/0022-3697(75)90192-4

Panlener, R. J., Blumenthal, R. N., and Garnier, J. E. (1975). A thermodynamic study of nonstoichiometric cerium dioxide. *J. Phys. Chem. Solids* 36 (11), 1213–1222. doi:10.1016/0022-3697(75)90192-4

Patankar, A. S., Wu, X.-Y., Choi, W., Tuller, H. L., and Ghoniem, A. F. (2022). A reactor train system for efficient solar thermochemical fuel production. *J. Sol. Energy Eng.* 144, 061014. doi:10.1115/1.4055298

Pérez, A., Orfila, M., Díaz, E., Linares, M., Sanz, R., Marugán, J., et al. (2024). Reticulated porous structures of La0.8Al0.2NiO3-δ perovskite for enhanced green hydrogen production by thermochemical water splitting. *Catal. Today* 442, 114919. doi:10.1016/j.cattod.2024.114919

Perraudin, D. Y. S., and Haussener, S. (2017). Numerical quantification of coupling effects for radiation-conduction heat transfer in participating macroporous media: investigation of a model geometry. *Int. J. Heat Mass Transf.* 112, 387–400. doi:10.1016/j.ijheatmasstransfer.2017.03.079

Polo, J., Poddar, S., Simal, N., Ballestrín, J., Marzo, A., Kay, M., et al. (2025). Solar tower power generation under future attenuation and climate scenarios. *Renew. Sustain. Energy Rev.* 207, 114997. doi:10.1016/j.rser.2024.114997

Qian, X., He, J., Mastronardo, E., Baldassarri, B., Wolverton, C., and Haile, S. M. (2020). Favorable redox thermodynamics of SrTi0.5Mn0.5O3−δ in solar thermochemical water splitting. *Chem. Mater.* 32 (21), 9335–9346. doi:10.1021/acs.chemmater.0c03278

Qian, X., He, J., Mastronardo, E., Baldassarri, B., Yuan, W., Wolverton, C., et al. (2021). Outstanding properties and performance of CaTi0.5Mn0.5O3−δ for solar-driven thermochemical hydrogen production. *Matter* 4 (2), 688–708. doi:10.1016/j.matt.2020.11.016

Richter, S., Grobbel, J., Brendelberger, S., Roeb, M., and Sattler, C. (2025). Particle mechanics and mixture homogeneity in a demonstration reactor system for the indirect reduction of redox particles. *Sol. Energy* 292, 113403. doi:10.1016/j.solener.2025.113403

Rojas, P., Alegría, N., and Toledo, M. (2025). Numerical and experimental investigation of a two-stage thermochemical water-splitting reactor based on a cerium oxide reduction–oxidation cycle. *Energy Convers. Manag.* 323, 119217. doi:10.1016/j.enconman.2024.119217

Safari, F., and Dincer, I. (2020). A review and comparative evaluation of thermochemical water splitting cycles for hydrogen production. *Energy Convers. Manag.* 205, 112182. doi:10.1016/j.enconman.2019.112182

Schäppi, R., Rutz, D., Dähler, F., Muroyama, A., Haueter, P., Lilliestam, J., et al. (2022). Drop-in fuels from sunlight and air. *Nature* 601 (7891), 63–68. doi:10.1038/s41586-021-04174-y

Scheffe, J. R., and Steinfeld, A. (2012). Thermodynamic analysis of cerium-based oxides for solar thermochemical fuel production. *Energy Fuels* 26 (3), 1928–1936. doi:10.1021/ef201875v

Scheffe, J. R., Weibel, D., and Steinfeld, A. (2013). Lanthanum–strontium–manganese perovskites as redox materials for solar thermochemical splitting of H2O and CO2. *Energy Fuels* 27 (8), 4250–4257. doi:10.1021/ef301923h

Scopus (2025). Empowering research with the world's leading abstract and citation database. Available online at: https://www.scopus.com/search/form.uri?display=basic#basic.

Scott, P., Patankar, A., Wu, Z., Haussmann, H., and Ghoniem, A. (2024). "High-fidelty thermomechnical modeling of a novel indirectly irradiated reactor for solar thermochemical fuel production," in *18th international conference on energy sustainability*. Anaheim, CA, USA.

Sedighi, M., Taylor, R. A., and Padilla, R. V. (2021). Experimentally validated pore-scale numerical analysis for high-temperature (>700 ℃), high-efficiency (>90%) volumetric solar receivers. *Energy Convers. Manag. X* 12, 100127. doi:10.1016/j.ecmx.2021.100127

Sharma, J. P., Kumar, R., Ahmadi, M. H., Mukhtar, A., Yasir, A. S. H. M., Sharifpur, M., et al. (2023). Chemical and thermal performance analysis of a solar thermochemical reactor for hydrogen production *via* two-step WS cycle. *Energy Rep.* 10, 99–113. doi:10.1016/j.egyr.2023.06.012

Shuai, Y., Zhang, H., Guene Lougou, B., Jiang, B., Mustafa, A., Wang, C. H., et al. (2021). Solar-driven thermochemical redox cycles of ZrO2 supported NiFe2O4 for CO2 reduction into chemical energy. *Energy* 223, 120073. doi:10.1016/j.energy.2021.120073

Shuai, Y., Guene Lougou, B., Zhang, H., Zhao, J., Ahouannou, C., and Tan, H. (2021). Heat transfer analysis of solar-driven high-temperature thermochemical reactor using NiFe-Aluminate RPCs. *Int. J. Hydrogen Energy* 46 (16), 10104–10118. doi:10.1016/j.ijhydene.2020.03.240

Singh, A., Lapp, J., Grobbel, J., Brendelberger, S., Reinhold, J. P., Olivera, L., et al. (2017). Design of a pilot scale directly irradiated, high temperature, and low pressure moving particle cavity chamber for metal oxide reduction. *Sol. Energy* 157, 365–376. doi:10.1016/j.solener.2017.08.040

Suter, S., Steinfeld, A., and Haussener, S. (2014). Pore-level engineering of macroporous media for increased performance of solar-driven thermochemical fuel processing. *Int. J. Heat Mass Transf.* 78, 688–698. doi:10.1016/j.ijheatmasstransfer.2014.07.020

Takacs, M., Scheffe, J. R., and Steinfeld, A. (2015). Oxygen nonstoichiometry and thermodynamic characterization of Zr doped ceria in the 1573–1773 K temperature range. *Phys. Chem. Chem. Phys.* 17 (12), 7813–7822. doi:10.1039/C4CP04916K

Takacs, M., Hoes, M., Caduff, M., Cooper, T., Scheffe, J. R., and Steinfeld, A. (2016). Oxygen nonstoichiometry, defect equilibria, and thermodynamic characterization of LaMnO3 perovskites with Ca/Sr A-site and Al B-site doping. *Acta Mater.* 103, 700–710. doi:10.1016/j.actamat.2015.10.026

Tang, Q., Ma, Y., and Huang, K. (2021). $Fe_3O_4/ZrO_2$ composite as a robust chemical looping oxygen carrier: a kinetics study on the reduction process. *ACS Appl. Energy Mater.* 4 (7), 7091–7100. doi:10.1021/acsaem.1c01152

Tapia, E., González-Pardo, A., Iranzo, A., Romero, M., González-Aguilar, J., Vidal, A., et al. (2019). Multi-tubular reactor for hydrogen production: CFD thermal design and experimental testing. *Processes* 7 (1), 31. doi:10.3390/pr7010031

Tran, J. T., Warren, K. J., Wilson, S. A., Muhich, C. L., Musgrave, C. B., and Weimer, A. W. (2024). An updated review and perspective on efficient hydrogen generation *via* solar thermal water splitting. *WIREs Energy Environ.* 13 (4), e528. doi:10.1002/wene.528

United Nations (2025). *Net zero coalition*'. NY, United States: United Nations. Available online at: https://www.un.org/en/climatechange/net-zero-coalition (Accessed on February 12, 2025).

Valadés-Pelayo, P. J., and Arancibia-Bulnes, C. A. (2017). Transient behavior of a multi-tubular cavity solar thermochemical reactor. *Appl. Therm. Eng.* 123, 1255–1262. doi:10.1016/j.applthermaleng.2017.05.192

Valades-Pelayo, P. J., Villafán-Vidales, H. I., Romero-Paredes, H., and Arancibia-Bulnes, C. A. (2017). Modeling of a tubular solar reactor for continuous reduction of CeO2: the effect of particle size and loading on radiative heat transfer and conversion. *Chem. Eng. Sci.* 162, 77–87. doi:10.1016/j.ces.2016.12.045

Valle-Hernández, J., Romero-Paredes, H., and Pacheco-Reyes, A. (2017). Modeling of the steam hydrolysis in a two-step process for hydrogen production by solar concentrated energy. *AIP Conf. Proc.* 1850 (1), 100016. doi:10.1063/1.4984473

Vega Puga, E., Brendelberger, S., Weber, A., and Sattler, C. (2024). Modeling development of a receiver–reactor of type R2Mx for thermochemical water splitting. *J. Sol. Energy Eng.* 146, 051011. doi:10.1115/1.4065975

Venstrom, L. J., De Smith, R. M., Bala Chandran, R., Boman, D. B., Krenzke, P. T., and Davidson, J. H. (2015). Applicability of an equilibrium model to predict the conversion of CO2 to CO *via* the reduction and oxidation of a fixed bed of cerium dioxide. *Energy Fuels* 29 (12), 8168–8177. doi:10.1021/acs.energyfuels.5b01865

Verlage, E., Hu, S., Liu, R., Jones, R. J. R., Sun, K., Xiang, C., et al. (2015). A monolithically integrated, intrinsically safe, 10% efficient, solar-driven water-splitting system based on active, stable earth-abundant electrocatalysts in conjunction with tandem III–V light absorbers protected by amorphous $TiO_2$ films. *Energy Environ. Sci.* 8 (11), 3166–3172. doi:10.1039/C5EE01786F

Vidal, A., and Martinez, D. (2020). An ageing protocol for testing high temperature solar materials for thermochemical applications. *Sol. Energ Mater Sol. Cells* 212, 110572. doi:10.1016/j.solmat.2020.110572

Villafán-Vidales, H. I., Abanades, S., Caliot, C., and Romero-Paredes, H. (2011). Heat transfer simulation in a thermochemical solar reactor based on a volumetric porous receiver. *Appl. Therm. Eng.* 31 (16), 3377–3386. doi:10.1016/j.applthermaleng.2011.06.022

Villafán-Vidales, H. I., Abanades, S., Arancibia-Bulnes, C. A., Riveros-Rosas, D., Romero-Paredes, H., Espinosa-Paredes, G., et al. (2012). Radiative heat transfer analysis of a directly irradiated cavity-type solar thermochemical reactor by Monte-Carlo ray tracing. *J. Renew. Sustain. Energy* 4 (4), 043125. doi:10.1063/1.4747825

Vyazovkin, S., Burnham, A. K., Criado, J. M., Pérez-Maqueda, L. A., Popescu, C., and Sbirrazzuoli, N. (2011). ICTAC kinetics committee recommendations for performing kinetic computations on thermal analysis data. *Thermochim. Acta* 520 (1–2), 1–19. doi:10.1016/j.tca.2011.03.034

Wang, B., Li, L., Pottas, J. J., Bader, R., Kreider, P. B., Wheeler, V. M., et al. (2020). Thermal model of a solar thermochemical reactor for metal oxide reduction. *J. Sol. Energy Eng.* 142, 051002. doi:10.1115/1.4046229

Wang, B., Li, L., Schäfer, F., Pottas, J. J., Kumar, A., Wheeler, V. M., et al. (2021). Thermal reduction of iron–manganese oxide particles in a high-temperature packed-bed solar thermochemical reactor. *Chem. Eng. J.* 412, 128255. doi:10.1016/j.cej.2020.128255

Wang, P., Wei, R. K., and Vafai, K. (2022). A dual-scale transport model of the porous ceria based on solar thermochemical cycle water splitting hydrogen production. *Energy Convers. Manag.* 272, 116363. doi:10.1016/j.enconman.2022.116363

Wang, P., Duan, R. M., Xu, R. N., and Jiang, P. X. (2024). Multi-field coupling and collaborative optimization design of the solar thermochemical cycle process based on ceria. *Appl. Therm. Eng.* 236, 121880. doi:10.1016/j.applthermaleng.2023.121880

Wang, L., Gao, Z., Xu, W., Chen, K., Zhu, L., Du, J., et al. (2025). Research on oxygen production characteristics in solar-driven CeO2 reduction. *J. Phys. Conf. Ser.* 2932 (1), 012013. doi:10.1088/1742-6596/2932/1/012013

Wei, L., Pan, Z., Shi, X., Esan, O. C., Li, G., Qi, H., et al. (2023). Solar-driven thermochemical conversion of H2O and CO2 into sustainable fuels. *iScience* 26, 108127. doi:10.1016/j.isci.2023.108127

Wei, L., Li, Z., Pan, Z., Yi, Z., Li, G., and An, L. (2024). A design of solar-driven thermochemical reactor integrated with heat recovery for continuous production of renewable fuels. *Energy Convers. Manag.* 310, 118484. doi:10.1016/j.enconman.2024.118484

Wenzel, M., Aditya Dharanipragada, N., Galvita, V. V., Poelman, H., Marin, G. B., Rihko-Struckmann, L., et al. (2017). CO production from CO2 *via* reverse water–gas shift reaction performed in a chemical looping mode: kinetics on modified iron oxide. *J. CO2 Util.* 17, 60–68. doi:10.1016/j.jcou.2016.10.015

Wheeler, V. M., Bader, R., Kreider, P. B., Hangi, M., Haussener, S., and Lipinski, W. (2017). Modelling of solar thermochemical reaction systems. *Sol. Energy* 156, 149–168. doi:10.1016/j.solener.2017.07.069

World Energy Outlook (2024). *World Energy Outlook*. IEA, Paris: International Energy Agency. Available online at: https://www.iea.org/reports/world-energy-outlook-2024.

Wu, Z., Caliot, C., Bai, F., Flamant, G., Wang, Z., Zhang, J., et al. (2010). Experimental and numerical studies of the pressure drop in ceramic foams for volumetric solar receiver applications. *Appl. Energy* 87 (2), 504–513. doi:10.1016/j.apenergy.2009.08.009

Xu, D., and Lin, M. (2023). Design controllable TPMS structures for solar thermal applications: a pore-scale vs. volume-averaged modeling approach. *Int. J. Heat Mass Transf.* 201, 123625. doi:10.1016/j.ijheatmasstransfer.2022.123625

Xu, R., and Wiesner, T. F. (2012). Dynamic model of a solar thermochemical water-splitting reactor with integrated energy collection and storage. *Int. J. Hydrogen Energy* 37 (3), 2210–2223. doi:10.1016/j.ijhydene.2011.10.053

Yang, C.-K., Yamazaki, Y., Aydin, A., and Haile, S. M. (2014). Thermodynamic and kinetic assessments of strontium-doped lanthanum manganite perovskites for two-step thermochemical water splitting. *J. Mater. Chem. A* 2 (33), 13612–13623. doi:10.1039/C4TA02694B

Yang, S., Li, L., Wang, B., Li, S., Wang, J., Lund, P., et al. (2021). Thermodynamic analysis of a conceptual fixed-bed solar thermochemical cavity receiver–reactor array for water splitting *via* Ceria redox cycling. *Front. Energy Res.* 9, 565761. doi:10.3389/fenrg.2021.565761

Yuan, C., Jarrett, C., Chueh, W. C., Kawajiri, Y., and Henry, A. (2016). A new solar fuels reactor using a liquid metal heat transfer fluid: modeling and sensitivity analysis. *J. Therm. Eng.* 2 (4), 837–852. doi:10.18186/jte.73311

Zhang, H., and Smith, J. D. (2019). Investigating influences of geometric factors on a solar thermochemical reactor for two-step carbon dioxide splitting *via* CFD models. *Sol. Energy* 188, 935–950. doi:10.1016/j.solener.2019.06.080

Zhang, H., and Smith, J. D. (2021). Modeling of ceria reduction in a solar thermochemical reactor *via* DEM method. *J. Energy Power Technol.* 3, 1–29. doi:10.21926/jept.2101008

Zhang, H., Guene Lougou, B., Pan, R., Shuai, Y., Wang, F., Cheng, Z., et al. (2018). Analysis of thermal transport and fluid flow in high-temperature porous media solar thermochemical reactor. *Sol. Energy* 173, 814–824. doi:10.1016/j.solener.2018.08.015

Zhang, H., Shuai, Y., Guene Lougou, B., Jiang, B., and Huang, X. (2020). Thermal characteristics and thermal stress analysis of solar thermochemical reactor under high-flux concentrated solar irradiation. *Sci. China Technol. Sci.* 63 (9), 1776–1786. doi:10.1007/s11431-019-1486-2

Zhao, Z., Uddi, M., Tsvetkov, N., Yildiz, B., and Ghoniem, A. F. (2016). Redox kinetics study of fuel reduced ceria for chemical-looping water splitting. *J. Phys. Chem. C* 120 (30), 16271–16289. doi:10.1021/acs.jpcc.6b01847

Zhao, L., Xu, D., Deng, S., and Lin, M. (2025a). Performance assessment of two-step solar thermochemical fuel production systems with a transient multi-scale model. *Energy Convers. Manag.* 334, 119821. doi:10.1016/j.enconman.2025.119821

Zhao, L., Xu, D., Feng, G., Zhou, D., Zhang, Y., Deng, S., et al. (2025b). Assessing redox material performance through a coupled reactor–system modeling framework for solar thermochemical hydrogen production. *Int. J. Hydrogen Energy* 170, 151163. doi:10.1016/j.ijhydene.2025.151163

Zinkevich, M., Djurovic, D., and Aldinger, F. (2006). Thermodynamic modelling of the cerium–oxygen system. *Solid State Ionics* 177 (11), 989–1001. doi:10.1016/j.ssi.2006.02.044

Zoller, S., Koepf, E., Roos, P., and Steinfeld, A. (2019). Heat transfer model of a 50 kW solar receiver–reactor for thermochemical redox cycling using cerium dioxide. *J. Sol. Energy Eng.* 141, 021014. doi:10.1115/1.4042059

Zoller, S., Koepf, E., Nizamian, D., Stephan, M., Patané, A., Haueter, P., et al. (2022). A solar tower fuel plant for the thermochemical production of kerosene from H2O and CO2. *Joule* 6 (7), 1606–1616. doi:10.1016/j.joule.2022.06.012

# Glossary

## List of symbols

| | |
|---|---|
| $d_{pore}$ | Mean pore diameter |
| $d_p$ | Particles diameter |
| $A_{sf}$ | Specific surface area |
| $R$ | Universal gas constant |
| $p_{O_2}$ | Oxygen partial pressure |
| $p_0$ | Reference pressure |
| $m_{load}$ | Reactive mass available |
| $r_i$ | Chemical source term of the $i^{th}$ species $[kg/m^3s]$ |
| $u$ | Velocity vector |
| $Re$ | Reynolds number |
| $S_{porous}$ | Momentum source term |
| $\Delta h_{red}$ | Specific enthalpy of reduction |
| $\Delta s_{red}$ | Specific entropy of reduction |
| $k$ | Reaction rate constant |
| $q_{rad}$ | Radiative heat flux [W/m$^2$] |

## Greek letters

| | |
|---|---|
| $\alpha$ | Absorption coefficient |
| $\beta$ | Extinction coefficient |
| $\delta$ | Non-stoichiometry |
| $\varepsilon$ | Porosity |
| $\kappa$ | Scattering coefficient |
| $\mu$ | Dynamic viscosity |
| $\rho$ | Density |
| $\sigma$ | Stefan Boltzmann constant |

## Acronyms

| | |
|---|---|
| **n.a** | Not available |
| **RTS** | Reactor train system |
| **Ppi** | Pores per inch |
| **LTE** | Local thermal equilibrium |
| **LTNE** | Local thermal non-equilibrium |
| **RTE** | Radiative heat transfer equation |
| **RDA** | Rosseland diffusion approximation |

## Subscripts

| | |
|---|---|
| **p** | Particle |
| **s** | Solid |
| **f** | Fluid |
| **eff** | Effective property |
| **Red** | Reduction |
| **ox** | Oxidation |